

Non-ideal MHD and protostellar feedback effects on disk formation and evolution in numerical simulations of star cluster formation

Nina Filippova¹*, Stella S. R. Offner¹, Michael Y. Grudić², and Philip F. Hopkins³

¹ Department of Astronomy, University of Texas at Austin, TX 78712, USA

² Center for Computational Astrophysics, Flatiron Institute, 162 5th Ave, New York, NY 10010, USA

³ TAPIR, Mailcode 350-17, California Institute of Technology, Pasadena, CA 91125, USA

Accepted XXX. Received YYY; in original form ZZZ

ABSTRACT

While recent surveys have resolved hundreds of nearby protostellar disks, numerical simulations assuming ideal magnetohydrodynamics (MHD) have historically struggled to achieve disk formation due to efficient angular momentum removal by magnetic torques. Non-ideal MHD effects, which become relevant at the low ionization fractions typical of molecular clouds, have been shown to reduce the effectiveness of magnetic braking and promote disk formation. In this work, we present the results from a suite of calculations following the gravitational collapse of $50 M_{\odot}$ turbulent molecular cloud cores down to the formation and evolution of stellar systems and protostellar disks. We use the radiation-MHD code GIZMO including non-ideal MHD (Ohmic resistivity, ambipolar diffusion, and the Hall effect) and the STARFORGE numerical framework for modeling star formation and stellar feedback. We compare the effects of assuming ideal vs. non-ideal MHD and including sub-grid protostellar jet feedback on disk formation and evolution. Disks form in all of our models but are least massive in the model with ideal MHD and sub-grid jet feedback. Apart from the ideal MHD+jets model, we do not observe any significant differences in disk properties between the ideal and non-ideal MHD models. Disk sizes are in general agreement with those of observed disks. Jet feedback increases core fragmentation and reduces final stellar masses. Our results suggest that magnetic braking does not efficiently suppress disk formation, regardless of whether ideal or non-ideal MHD is assumed, under the dynamical conditions in which multiple stellar systems form.

Key words: methods: numerical – MHD – protoplanetary discs – stars: formation – stars: jets – stars: winds, outflows

1 INTRODUCTION

Stars form during the gravitational collapse of dense clouds of gas and dust, a process that is inhibited by the turbulent, magnetic, and thermal support within the cloud (McKee & Ostriker 2007). Angular momentum conservation during the collapse produces a rotationally-supported disk around the growing protostar, which funnels mass to the protostar as well as provides raw material for planet formation (Zhao et al. 2020a). Recent surveys by the Very Large Array (VLA) and the Atacama Large Millimeter/submillimeter Array (ALMA) have resolved disks around hundreds of protostars, suggesting that their formation is a regular occurrence during the collapse process (Tobin et al. 2020). Protostellar disk formation is observed in numerical calculations as well. Bate (2018) presented the first population synthesis study of protostellar disks formed in a radiation hydrodynamical simulation of star cluster formation, reporting the statistical properties (such as typical disk sizes) of a diverse population of >100 disks formed over $\sim 10^5$ years of protostellar evolution in a $500 M_{\odot}$ cloud. However, numerical simulations have historically struggled to achieve disk formation once even relatively modest magnetic fields are included (see, e.g., Joos et al. 2012; Santos-Lima et al. 2012), largely due to the efficient removal of angular momentum from the

disk that occurs under the assumptions of ideal magnetohydrodynamics (MHD). As observations suggest that molecular clouds are threaded by large-scale magnetic fields on the order of ~ 10 – $100 \mu\text{G}$ (Crutcher 2012), this failure to form disks in magnetized models points to a significant challenge in disk formation theory.

It is clear that angular momentum cannot be perfectly conserved during the collapse. Observations of star-forming clouds measure a typical specific angular momentum of $j \approx 10^{21} \text{ cm}^2 \text{ s}^{-1}$ (e.g., Goodman et al. 1993), while stellar cores have a typical specific angular momentum of $j \approx 10^{15} \text{ cm}^2 \text{ s}^{-1}$ (e.g., Belloche 2013), a difference of six orders of magnitude that has been referred to as the “angular momentum problem.” Angular momentum may be removed from the core by magnetic (as well as gravitational) torques (see, e.g., the review by Wurster & Li 2018). The presence of charged species – ions, electrons, and charged dust grains – in the star-forming gas causes the fluid motion to become coupled to the magnetic field dynamics. The rotation of the collapsing material drags the magnetic field lines along the direction of rotation, creating a magnetic tension force, and thereby a torque, which counteracts the overall rotation. In the limit of ideal MHD, in which the relative drift between different charged species is neglected, the perfect coupling between the fluid and the field means that even moderate magnetic field strengths can lead to very efficient angular momentum removal and the so-called

* E-mail: ninaf@utexas.edu (NF)

“magnetic braking catastrophe” (see, e.g., Zhao et al. 2020a; Maury et al. 2022, and sources within), suppressing disk formation entirely.

Theoretical and numerical studies aimed at resolving the magnetic braking catastrophe have considered adjustments such as introducing misalignment between the magnetic field and the axis of rotation (e.g., Gray et al. 2018; Hirano et al. 2020), adding turbulence (e.g., Santos-Lima et al. 2012; Joos et al. 2013; Lewis & Bate 2018), or including non-ideal MHD effects (e.g., Wurster et al. 2019; Zhao et al. 2020b, 2021). Molecular clouds are only partially ionized (with an ionization fraction n_e/n_H ranging from 10^{-4} at the cloud boundary down to 10^{-9} in the densest cores; see, e.g., Goicoechea et al. 2009), and so non-ideal MHD effects, such as Ohmic resistivity (electron-ion/neutral drift), ambipolar diffusion (ion-neutral drift), and the Hall effect (ion-electron drift) become increasingly relevant. These effects relax the fluid-field coupling: Ohmic resistivity and ambipolar diffusion act as dissipative terms which weaken the magnetic field, while the Hall effect serves as a dispersive term which modifies the magnetic field line geometry. The influence of each term depends on the local density and temperature, as well as microphysics such as the dust grain size distribution and local cosmic ray ionization rate (Zhao et al. 2020a, 2021; Wurster 2021). The Hall effect has been the most challenging to implement numerically, and is the most recent to be included in such studies.

The classical approach to modeling star formation, pioneered by Larson (1969), begins with the assumption of an isolated spherical core which collapses due to its own gravity. Early numerical studies of protostellar disk formation adopted this model, typically beginning with a $\sim 1 M_\odot$ uniform-density sphere and investigating the effects of including additional physics, such as rotation, turbulence, magnetic fields, and non-ideal MHD, on disk formation outcomes (see the review by Kuffmeier 2024). These simplified models, while suitable for studying the effects of various parameters on core and disk evolution in a well-defined setup, fail to capture the dynamical conditions in which stars form. Observations suggest that the morphology of prestellar cores embedded in dense filaments in Giant Molecular Clouds (GMCs) deviate strongly from spherical symmetry (André et al. 2014; Kainulainen et al. 2017; Pineda et al. 2023; Hacar et al. 2023). Additionally, there is increasing evidence for large-scale asymmetric features, or ‘streamers’ (see the review by Pineda et al. 2023), as well as late-stage infall (e.g., Ginski et al. 2021), which continue to contribute mass even after the initial envelope mass reservoir has been depleted. And while our familiar solar system contains just one star, observations suggest that this is the exception, rather than the rule. Most stars form in systems consisting of multiple gravitationally-bound stars at sub-parsec separations, with the multiplicity fraction monotonically increasing with the mass of the primary star (Offner et al. 2022). Furthermore, most multiple systems form and evolve into their final configuration by the end of the mass accretion stage (Offner et al. 2022). Several mechanisms have been proposed to explain the formation of multiple stellar systems, such as the migration of existing protostars (e.g., Ostriker 1994; Moeckel & Bally 2007; Bate 2012), the fragmentation of cloud substructures such as cores and filaments (e.g., Larson 1972; Tomisaka 2014; Guszejnov & Hopkins 2015; Guszejnov et al. 2017), and the fragmentation of the protostellar disk itself (e.g., Adams et al. 1989; Shu et al. 1990; Bonnell 1994). Interactions between young stars are common during the first Myr of cluster evolution (Pfalzner 2013). So-called stellar ‘flybys’ have been shown to truncate disk sizes and induce misalignment between the disk and protostellar rotation axes. Once stars form, stellar feedback in the form of radiation, jets, winds, and supernovae affects subsequent star formation and cloud evolution (e.g., Kim et al. 2021; Grudić et al. 2022).

A proper treatment of star (and disk) formation including stellar feedback and dynamical interactions in a turbulent, magnetized plasma must consider complex, non-linear physical processes spanning large dynamical ranges. Considerable improvements in both physical realism as well as computational efficiency over the last decade have made it feasible to attempt to study protostellar disk formation, not only in small ($1 M_\odot$), rotating, single-protostellar/disk models, but also in turbulent, magnetized cloud cores ($\sim 10\text{--}100 M_\odot$), which form stellar clusters and include various feedback mechanisms. In this paper, we present results from radiation ideal/non-ideal MHD simulations of low-mass cluster formation using the GIZMO code, comparing disk formation outcomes between models with ideal and non-ideal MHD. We also consider the effects of including sub-grid protostellar jet feedback. While self-consistently launched jets are not observed in most of our models, jet feedback has been shown to lead to an overall reduction in protostellar masses, as well as inject significant energy and momentum into the local star-forming environment (e.g., Guszejnov et al. 2021). It is very probable that such feedback affects disk formation and evolution as well.

2 METHODS

We model the gravitational collapse of a $M_0 = 50 M_\odot$ turbulent molecular cloud core (hereafter referred to as a cloud for notational convenience) down to the formation and evolution of a star cluster using the 3D radiation MHD code GIZMO, supplemented with modules for non-ideal MHD effects such as Ohmic resistivity, ambipolar diffusion and the Hall effect, as well as additional sink particle formation and feedback modules developed within the STARFORGE numerical framework (Hopkins 2015; Hopkins & Raives 2016; Hopkins 2017; Grudić et al. 2021). We use $N_{\text{gas}} = 5 \times 10^6$ equal-mass ($\Delta m = 10^{-5} M_\odot$) discretized fluid cells to simulate the evolution of the cloud using GIZMO’s Meshless Finite Mass (MFM) solver, in which the cells move with the local fluid velocity while maintaining fixed mass in a quasi-Lagrangian manner. This meshless method maintains exact mass, energy and momentum conservation; exhibits superior angular momentum conservation relative to grid methods; does not require artificial diffusion or viscosity terms; and is automatically adaptive in resolution (see Hopkins 2015, for details).

The initial cloud size and mass resolution are selected with the aim of resolving protostellar disk behavior within the context of multiple star formation in a realistic turbulent environment. Both parameters are comparable to those used in recent non-ideal MHD 3D SPH studies of cluster and disk formation (e.g., the $50 M_\odot$, $\Delta m = 10^{-5} M_\odot$ SPH calculations of Wurster et al. 2019).

Our models include three different sets of MHD physics: ideal MHD (labeled “ideal”), non-ideal MHD with Ohmic resistivity and ambipolar diffusion (“non-ideal OA”), and non-ideal MHD with Ohmic resistivity, ambipolar diffusion and the Hall effect (“non-ideal OAH”). As the Hall effect has been the most challenging to implement numerically, several previous studies investigating the role of non-ideal MHD in protostellar disk formation did not include the Hall effect; we therefore include calculations both with and without the Hall effect for comparison. For each set of MHD physics, we perform one calculation with no sub-grid STARFORGE protostellar jet feedback and one with jet feedback (appending “+jets” to the model label), resulting in six calculations of cloud evolution. The computational cost of each model ranges from 4224 to 5736 CPU

Cloud parameters	
M_0	$50 M_\odot$
R_0	0.3077 pc
ρ_0	$2.77 \times 10^{-20} \text{ g cm}^{-3}$
Σ_0	$168 M_\odot \text{ pc}^{-2}$
T_0	20 K
$c_{s,0}$	0.2 km s ⁻¹
$\sigma_{3D,0}$	0.648 km s ⁻¹
α_0	1.0
B_0	$5.41 \times 10^{-6} \text{ G}$
μ_0	13.3
t_{ff}	0.4 Myr
t_{cross}	0.465 Myr

Table 1. Initial cloud parameters: mass (M_0), radius (R_0), mass density (ρ_0), surface density (Σ_0), temperature (T_0), sound speed ($c_{s,0}$), 3D rm velocity dispersion ($\sigma_{3D,0}$), turbulent virial parameter (α_0), magnetic field strength (B_0), mass-to-magnetic-flux ratio (μ_0), freefall time (t_{ff}), and turbulent crossing time (t_{cross}).

hours (corresponding to one hour of compute time on one node).¹ We use the Frontera supercomputer at the Texas Advanced Computing Center (TACC) for our calculations.

2.1 Initial conditions

The cloud radius and velocity dispersion are chosen to satisfy the observed Larson size-linewidth relation for molecular clouds (MCs), $\sigma_{1D} \simeq 0.72 R_{\text{pc}}^{0.5}$ (e.g., Solomon et al. 1987; Finn et al. 2022), where R_{pc} is the radius in parsecs and σ_{1D} is the 1D turbulent velocity dispersion. The virial parameter is related to the velocity dispersion via

$$\alpha = \frac{5\sigma_{1D}^2 R_0}{GM_0}, \quad (1)$$

so specifying a turbulent virial parameter $\alpha_{\text{vir}} = 1.0$ leads to $R_0 = 0.3077$ pc, for an initial surface density of $\Sigma_0 = M_0/(\pi R_0^2) = 168 M_\odot/\text{pc}$ and mass density $\rho_0 = 2.77 \times 10^{-20} \text{ g cm}^{-3}$. Table 1 summarizes the initial cloud parameters, while Table 2 contains the relevant simulation settings.

Since it is currently infeasible to model resolved star formation in a fully Galactic context, MC simulations must assume some initial and boundary conditions, typically informed by theory and observations of MCs and the turbulent interstellar medium (ISM) in general. Popular approaches for setting these conditions for MCs have included a uniform-density sphere with a Gaussian random velocity field with a $\propto k^{-2}$ power spectrum to emulate turbulence and outflow boundary conditions (“SPHERE”; e.g., Bate et al. 2003), as well as a periodic box in which turbulence is first “stirred” for some period of time and allowed to reach a self-consistent initial turbulent state before self-gravity is switched on (“BOX”; e.g., Mac Low 1999). The SPHERE configuration, however, fails to capture nonlinear, fully-developed turbulence, while the BOX configuration encounters issues once stellar feedback is included, as the periodic boundary conditions force

¹ Including non-ideal MHD moderately increases the computational cost; the nonideal Ohmic+AD+Hall model runs ~20% slower than the ideal MHD model once the gas density reaches $\rho \gtrsim 10^{-14} \text{ g cm}^{-3}$. The remaining difference in computational cost between models is mostly due to the formation of tight binaries and multiple systems in several models, requiring short timesteps.

Simulation parameters	
L_{box}	$10 R_0$
ρ_{amb}	$0.01 \rho_0$
N_{gas}	5×10^6
Δm	$1 \times 10^{-5} M_\odot$
Δm_w	$0.1 \Delta m$
R_{sink}	0.5 AU
n_{crit}	$2 \times 10^{14} \text{ cm}^{-3}$
a_g	0.1 μm
ρ_g	3 g cm^{-3}
$\zeta_{\text{CR},0}$	$1.6 \times 10^{-17} \text{ s}^{-1}$

Table 2. Simulation parameters: box size (L_{box}), density of the surrounding ambient medium (ρ_{amb}), number of gas cells in the cloud (N_{gas}), mass resolution (Δm), mass launched by jets (Δm_w), sink particle radius (R_{sink}), critical density for star formation (n_{crit}), dust grain radius (a_g), dust grain density (ρ_g), and (unattenuated) cosmic ray ionization rate ($\zeta_{\text{CR},0}$).

TURBSPHERE parameters	
v_{drive}	0.5 km s ⁻¹
t_{coher}	0.602 Myr
λ_{\min}	0.15 pc
λ_{\max}	0.60 pc
seed	42

Table 3. TURBSPHERE turbulent driving parameters: turbulent driving rms velocity (v_{drive}), turbulent driving coherence time (t_{coher}), minimum wavelength (λ_{\min}), maximum wavelength (λ_{\max}), random turbulent seed (seed).

any ejected material to remain within the simulation volume. We choose to use instead the TURBSPHERE initialization setup of Lane et al. (2022), which combines the SPHERE benefits of a spatially-localized density distribution and outflowing boundary conditions with the BOX advantage of fully-developed turbulence.

The turbulent initial conditions for the clouds are generated by running the TURBSPHERE setup (in which self-gravity is disabled and the gas is confined by an analytic potential while being continuously stirred to model the turbulent energy cascade down from larger scales; see Lane et al. 2022, for details) for three turbulent crossing times, $t_{\text{cross}} = R_0/\sigma_{1D}$. Under this setup, the resulting cloud achieves a quasi-equilibrium state with the desired hallmarks of supersonic turbulence within a few t_{cross} , at which point self-gravity is enabled, turbulent driving is disabled, and the star-forming calculations begin. Table 3 summarizes the turbulent driving parameters used in the TURBSPHERE configuration.

For a uniform magnetic field of magnitude $|\mathbf{B}| = B$ in a static cloud, the magnetic support against gravitational collapse can be estimated by comparing the mass-to-magnetic flux ratio to a critical value,

$$\mu_\Phi = \frac{(M/\Phi_B)}{(M/\Phi_B)_{\text{crit}}}, \quad (2)$$

where $\Phi_B = \pi R^2 B$ is the magnetic flux through a spherical cloud of radius R , and, following Mouschovias & Spitzer (1976), we define the critical mass-to-flux ratio as

$$\left(\frac{M}{\Phi_B} \right)_{\text{crit}} \approx \frac{0.53}{3\pi} \sqrt{\frac{5}{G}}, \quad (3)$$

where G is the gravitational constant. In terms of the gravitational potential energy E_{grav} and magnetic energy E_{mag} of a uniform-

density spherical cloud,

$$\mu_\Phi \approx \frac{1}{0.53\sqrt{2}} \sqrt{\frac{|E_{\text{grav}}|}{E_{\text{mag}}}} \approx 1.33 \sqrt{\frac{|E_{\text{grav}}|}{E_{\text{mag}}}}. \quad (4)$$

We use Eq. 4 to estimate μ_Φ once the cloud is no longer uniformly spherical, e.g., at the conclusion of the TURBS SPHERE calculations, by directly calculating E_{grav} and E_{mag} for the gas.² The initial magnetic field has a uniform magnitude $B_0 = 5.41 \times 10^{-6}$ G in the z -direction, corresponding to an initial normalized mass-to-flux ratio $\mu_\Phi = 13.3$, or $E_{\text{mag}} = 0.01|E_{\text{grav}}|$; however, after $\sim 3 t_{\text{cross}}$, the higher-density gas ($\rho \gtrsim 10^{-20}$ g cm $^{-3}$) has an average magnetic field strength of $B \simeq 1.85 \times 10^{-5}$ G ($\mu_\Phi \simeq 2.4$) in the ideal MHD case and an average magnetic field strength of $B \simeq 1.86 \times 10^{-5}$ G ($\mu_\Phi = 2.5$) in the non-ideal MHD calculations including Ohmic dissipation and ambipolar diffusion. These clouds are magnetically supercritical ($\mu_\Phi > 1$), meaning that magnetic support is insufficient to prevent collapse.

2.2 Non-ideal MHD

Magnetohydrodynamics (MHD) describes the joint dynamics of magnetic fields and gas flows. As long as the fluid approximation holds, an astrophysical plasma can be described using a multifluid approach, where each species (e.g., ions, neutrals, electrons, and charged dust grains) has its own continuity, momentum, and energy equation, coupled by interaction terms describing the collisions between different species. Under several standard assumptions, such as local quasineutrality (i.e., ion and electron number densities are approximately equal; $n_i \approx n_e = n$) and negligible electron inertia relative to the ion and neutral inertia (i.e., letting $m_e \rightarrow 0$), the multifluid equations can be simplified to the standard single-fluid MHD description. The ideal MHD approximation further assumes a perfectly-conducting fluid, and neglects the drift velocities between different charged species. Although widely used in astrophysical studies, the assumptions used to derive the ideal MHD equations can break down, particularly in regions with low ionization fractions (such as protostellar disks, where $x_e = n_e/n_H \lesssim 10^{-10}$; see, e.g., disk models by [Lesur et al. 2014](#)).

Non-ideal MHD takes into account collisions between different charged species, and in astrophysical contexts is typically parameterized via Ohmic dissipation (collisions with electrons), the Hall effect (ion-electron drift), and ambipolar diffusion (ion-neutral drift). As the mass density and momentum exchange of the fluid is dominated by the neutral gas, the “strong coupling” assumption typically holds, under which the main difference between the ideal and non-ideal MHD equations lies in the induction equation:

$$\begin{aligned} \frac{\partial \mathbf{B}}{\partial t} &= \frac{\partial \mathbf{B}}{\partial t} \Big|_{\text{ideal}} + \frac{\partial \mathbf{B}}{\partial t} \Big|_{\text{non-ideal}} \\ &= \nabla \times (\mathbf{v} \times \mathbf{B}) \\ &\quad - \nabla \times \{ \eta_O \mathbf{J} + \eta_H (\mathbf{J} \times \hat{\mathbf{B}}) + \eta_A [\hat{\mathbf{B}} \times (\mathbf{J} \times \hat{\mathbf{B}})] \}, \end{aligned} \quad (5)$$

² Previous STARFORGE calculations (e.g., [Guszejnov et al. 2020, 2021](#)) define $\mu_\Phi \approx 0.4\sqrt{|E_{\text{grav}}|/E_{\text{mag}}}$, which is smaller than μ_Φ in Eq. 4 by approximately a factor of π ; the fiducial STARFORGE calculations with $E_{\text{mag}} = 0.01|E_{\text{grav}}|$ which are reported as having a mass-to-flux ratio of $\mu_\Phi = 4.2$ should in fact have $\mu_\Phi = 13.3$ to be consistent with the definition in [Mouschovias & Spitzer \(1976\)](#). Our Eq. 4 is consistent with the mass-to-flux ratio as used in similar studies (e.g., [Wurster et al. 2019; Lebreuilly et al. 2024a,b](#)).

where $\mathbf{J} \equiv \nabla \times \mathbf{B}$, $\hat{\mathbf{B}} \equiv \mathbf{B}/|\mathbf{B}|$, and η_O , η_H , and η_A are the Ohmic, Hall, and ambipolar resistivities. All of the microphysics governing species properties and interactions is contained in the η coefficients, with dependencies

$$\eta \equiv \eta(\rho, T, B, n_j, m_j, eZ_j), \quad (6)$$

where ρ and T are the gas density and temperature, B is the magnetic field strength, and n_j , m_j , and eZ_j are the number density, mass, and electric charge of species j .

The numerical methods for the non-ideal terms in GIZMO are presented and tested in [Hopkins \(2017\)](#). Ohmic dissipation and ambipolar diffusion are diffusive terms; diffusion is handled in an operator-split manner from the ideal MHD equation. The Hall effect is a dispersive term, but is handled similarly. The non-ideal MHD coefficients are dynamically calculated based on the local plasma state of the gas. The general expressions for the non-ideal coefficients are given by (e.g., [Wardle 2007](#))

$$\eta_O \equiv \frac{c^2}{4\pi\sigma_O}, \quad (7)$$

$$\eta_H \equiv \frac{c^2}{4\pi\sigma_\perp} \frac{\sigma_H}{\sigma_\perp}, \quad (8)$$

$$\eta_A \equiv \frac{c^2}{4\pi\sigma_\perp} \frac{\sigma_P}{\sigma_\perp} - \eta_O = \frac{c^2}{4\pi\sigma_O} \frac{\sigma_O\sigma_P - \sigma_\perp^2}{\sigma_\perp^2} \equiv \frac{c^2}{4\pi\sigma_O} \frac{\sigma_A}{\sigma_\perp^2}, \quad (9)$$

where σ_O , σ_H , and σ_P are the Ohmic, Hall, and Pedersen conductivities, and $\sigma_\perp = \sqrt{\sigma_H^2 + \sigma_P^2}$ is the total conductivity perpendicular to the magnetic field. The conductivities are given by (e.g., [Wardle & Ng 1999; Wardle 2007](#))

$$\sigma_O \equiv \frac{ec}{B} \sum_j n_j |Z_j| \beta_j, \quad (10)$$

$$\sigma_H \equiv \frac{ec}{B} \sum_j \frac{n_j Z_j}{1 + \beta_j^2}, \quad (11)$$

$$\sigma_P \equiv \frac{ec}{B} \sum_j \frac{n_j |Z_j| \beta_j}{1 + \beta_j^2}. \quad (12)$$

In the conductivities, β_j is the Hall parameter for species $j \in \{i, e, g\}$, which describes the relative magnitude between the magnetic forces and neutral drag. We use a modified form of the Hall parameter for β_e and β_i , as in [Wurster et al. \(2016\)](#), so that

$$\beta_e \equiv \frac{|Z_e| e B}{m_e c} \frac{1}{\nu_{ei} + \nu_{en}}, \quad (13)$$

$$\beta_i \equiv \frac{|Z_i| e B}{m_i c} \frac{1}{\nu_{ie} + \nu_{in}}, \quad (14)$$

$$\beta_g \equiv \frac{|Z_g| e B}{m_g c} \frac{1}{\nu_{gn}}, \quad (15)$$

where ν_{jk} are the collision frequencies between different species. With these modifications, we recover η_O from [Pandey & Wardle \(2008\)](#) and [Keith & Wardle \(2014\)](#), under the assumption $\beta_i \ll \beta_e$.

We note that while σ_O and σ_P are exclusively positive, σ_H may take negative values. To prevent $\eta_A \lesssim 0$ due to numerical round-off error when $\sigma_O\sigma_P \approx \sigma_\perp^2$, we follow [Wurster \(2016\)](#) and use a positive-definite formulation for η_A , calculating $\sigma_A = \sigma_O\sigma_P - \sigma_\perp^2$ as follows:

$$\sigma_A = \left(\frac{ec}{B} \right)^2 \sum_{j>k} \left[\frac{n_j |Z_j| \beta_j}{1 + \beta_j^2} \frac{n_k |Z_k| \beta_k}{1 + \beta_k^2} \right] \times \left(\frac{Z_k \beta_k}{|Z_k|} - \frac{Z_j \beta_j}{|Z_j|} \right)^2. \quad (16)$$

Here, $Z_i = +1$, $Z_e = -1$, $Z_n = 0$, and Z_g are the mean

ion/electron/neutral/dust grain charges, m_j and n_j the mass and number density of each species, e the electron charge, and c the speed of light. The neutral mass $m_n = \mu_p m_p$ is calculated using the appropriate mean molecular weight μ_p for the electron abundances, temperature, and molecular fraction determined in the cooling chemistry (for further details about the cooling chemistry see Hopkins et al. 2023). The grain mass is

$$m_g = \frac{4\pi}{3} a_g^3 \rho_g, \quad (17)$$

where $a_g = 0.1 \text{ }\mu\text{m}$ is the assumed grain radius and $\rho_g = 3 \text{ g cm}^{-3}$ the internal grain material density (typical of both silicate and carbonaceous grains). At the low temperatures and high densities typical of protostellar disks, ions are assumed to be dominated by Mg, so $m_i = 24.3m_p$ (Pollack et al. 1994). We use a mean number density $n \approx n_n = \rho/m_n$. The dust grain number density is proportional to the total number density (Keith & Wardle 2014):

$$n_g = \left(\frac{m_n}{m_g} \right) f_{dg} n, \quad (18)$$

where the fiducial dust-to-gas ratio is $f_{dg} = 0.01$ (Z/Z_\odot), but decreases above a sublimation temperature $T_{\text{dust}} = 1500 \text{ K}$, adopted from Isella & Natta (2005), and fit to the model by Pollack et al. (1994); in practice $f_{dg} \approx 0.01$ throughout the protostellar envelope and disk.

The collision frequencies, ν , are empirically calculated rates. The electron-ion rate is given by (Pandey & Wardle 2008)

$$\nu_{ei} = 0.051 n_e \left(\frac{T}{100 \text{ K}} \right)^{-1.5} \text{ s}^{-1}, \quad (19)$$

while the ion-electron rate is given by $\nu_{ie} = \frac{\rho_e}{\rho_i} \nu_{ei}$. The plasma-neutral collision frequencies are given by

$$\nu_{jn} = \frac{\langle \sigma v \rangle_{jn}}{m_n + m_j} \rho_n, \quad (20)$$

where $\langle \sigma v \rangle_{jn}$ is the rate coefficient for the momentum transfer by collisions of particles of type j with neutrals. The neutrals are assumed to be comprised of hydrogen and helium, with mass fractions $X \approx 0.76$ and $Y \approx 0.24$. For electron-neutral collisions, the rate coefficient is then

$$\langle \sigma v \rangle_{en} = X \langle \sigma v \rangle_{e-\text{H}_2} + Y \langle \sigma v \rangle_{e-\text{He}}, \quad (21)$$

where, following Pinto & Galli (2008), we use

$$\langle \sigma v \rangle_{e-\text{H}_2} = 3.16 \times 10^{-11} \left(\frac{v_{\text{rms}}}{\text{km s}^{-1}} \right)^{1.3} \text{ cm}^3 \text{ s}^{-1}, \quad (22)$$

$$\langle \sigma v \rangle_{e-\text{He}} = 7.08 \times 10^{-11} \left(\frac{v_{\text{rms}}}{\text{km s}^{-1}} \right)^{1.0} \text{ cm}^3 \text{ s}^{-1}, \quad (23)$$

with

$$v_{\text{rms}} = \sqrt{v_d + \frac{8k_B T}{\pi \mu_{en}}} \approx \sqrt{\frac{8k_B T}{\pi m_e}}, \quad (24)$$

k_B being the Boltzmann constant, where we assume that the electron-neutral drift velocity is $v_d = 0$ and that the electron-neutral reduced mass μ_{en} is approximately

$$\mu_{en} = \frac{m_e m_n}{m_e + m_n} \approx m_e. \quad (25)$$

Substituting for v_{rms} , the electron-neutral collision frequency we use

is

$$\nu_{en} = \left[5.15 \times 10^{-9} \left(\frac{T}{100 \text{ K}} \right)^{0.65} + 1.06 \times 10^{-9} \left(\frac{T}{100 \text{ K}} \right)^{0.5} \right] \left(\frac{\rho_n}{m_n + m_e} \right) \text{ s}^{-1}. \quad (26)$$

The ion-neutral rate coefficient is (Pinto & Galli 2008)

$$\langle \sigma v \rangle_{in} = 2.81 \times 10^{-9} Z_i^{1/2} \left[X \left(\frac{p_{\text{H}_2}}{\text{\AA}^3} \right)^{0.5} \left(\frac{\mu_{i-\text{H}_2}}{m_p} \right)^{-0.5} + Y \left(\frac{p_{\text{He}}}{\text{\AA}^3} \right)^{0.5} \left(\frac{\mu_{i-\text{He}}}{m_p} \right)^{-0.5} \right] \text{ cm}^3 \text{ s}^{-1}, \quad (27)$$

where the values of the polarizability are $p_{\text{H}_2} = 0.804 \text{ \AA}^3$ and $p_{\text{He}} = 0.207 \text{ \AA}^3$ (Osterbrock 1961), and $\mu_{i-\text{H}_2}$, $\mu_{i-\text{He}}$ are the ion-hydrogen and ion-helium reduced masses. The ion-neutral collision frequency used is then

$$\nu_{in} = \left[1.91 \times 10^{-9} \left(\frac{\mu_{i-\text{H}_2}}{m_p} \right)^{-0.5} + 0.31 \times 10^{-9} \left(\frac{\mu_{i-\text{He}}}{m_p} \right)^{-0.5} \right] \left(\frac{\rho_n}{m_n + m_i} \right) \text{ s}^{-1}. \quad (28)$$

For grain-neutral collisions, the rate coefficient is given by (Wardle & Ng 1999; Pinto & Galli 2008)

$$\nu_{gn} = \frac{4\pi}{3} a_g^2 \delta_{gn} \left(\frac{8k_B T}{\pi m_n} \right)^{0.5} \left(\frac{\rho_n}{m_n + m_g} \right) \text{ s}^{-1}, \quad (29)$$

where $\delta_{gn} \approx 1.3$ is the Epstein coefficient for spherical grains (Liu et al. 2003).

We assume the dust grains to have a non-evolving single grain size with primarily collisional and cosmic-ray charging. The electron and ion number densities vary as (e.g., Umebayashi & Nakano 1980; Fujii et al. 2011)

$$\frac{dn_i}{dt} = \zeta n - k_{ei} n_e n_i - k_{ig} n_i n_g, \quad (30)$$

$$\frac{dn_e}{dt} = \zeta n - k_{ei} n_e n_i - k_{eg} n_e n_g, \quad (31)$$

where ζ is the ionization rate and k_{jk} are the charge capture rates. We follow Keith & Wardle (2014) in assuming that recombination is inefficient, such that charge captures by grains dominate (i.e., $k_{ei} = 0$), and that we have an approximately steady-state system (i.e., $\frac{dn_i}{dt} \approx \frac{dn_e}{dt} \approx 0$). This allows us to calculate the ion and electron number densities as

$$n_i = \frac{\zeta n}{k_{ig} n_g}, \quad (32)$$

$$n_e = \frac{\zeta n}{k_{eg} n_g}. \quad (33)$$

For $Z_g < 0$ (as is typically the case), the charge capture rates are (Fujii et al. 2011)

$$k_{ig} \equiv \pi a_g^2 \left(\frac{8k_B T}{\pi m_i} \right)^{1/2} (1 + \psi), \quad (34)$$

$$k_{eg} \equiv \pi a_g^2 \left(\frac{8k_B T}{\pi m_e} \right)^{1/2} \exp(-\psi), \quad (35)$$

where ψ is related to the dust grain charge as $Z_g = -\psi \frac{a_g k_B T}{e^2}$. For

a given n and T and assuming charge neutrality, we construct the following equation to solve for ψ (and hence Z_g):

$$\psi = \alpha \left(\exp(\psi) - \frac{(m_i/m_e)^{1/2}}{1 + \psi} \right), \quad (36)$$

where

$$\alpha \equiv \frac{\zeta e^2 m_e^{1/2} m_g^2}{(8\pi)^{1/2} a_g^3 f_{dg} (k_B T)^{3/2} m_n^2 n}. \quad (37)$$

At the high densities typical of protostellar disks, we assume that cosmic rays are the dominant ionizing source, so that $\zeta = \zeta_{\text{CR}}$. When cosmic ray transport is not explicitly modeled, we mimic the empirical cosmic ray attenuation in dense molecular clouds, where observed column density ratios of molecular ions suggest that the cosmic ray ionization rate decreases as roughly $\zeta_{\text{CR}} \propto N_{\text{H}}^{-1}$ for $N_{\text{H}} \geq 10^{21} \text{ cm}^{-2}$ (Neufeld & Wolfire 2017). Following Kim et al. (2023), we initialize the simulations with an unattenuated cosmic ray ionization rate $\zeta_{\text{CR},0} = 1.6 \times 10^{-17} \text{ s}^{-1}$ (typical of the Solar environment; Cummings et al. 2016), and attenuate this rate according to the local column density. We estimate the column density N_{H} from a local scale-length approximation $N_{\text{H}} \approx \rho^2 X / (m_p \|\nabla \rho\|)$. The local cosmic ray ionization rate per H nucleon is then calculated as

$$\zeta_{\text{CR}} = \begin{cases} \zeta_{\text{CR},0}, & \text{if } N_{\text{H}} \leq N_{\text{H},0}, \\ \zeta_{\text{CR},0} \left(\frac{N_{\text{H}}}{N_{\text{H},0}} \right)^{-1} \exp \left(-\frac{N_{\text{H}} \cdot (m_p/X)}{\Sigma_{\text{CR},0}} \right), & \text{if } N_{\text{H}} > N_{\text{H},0}, \end{cases} \quad (38)$$

where $N_{\text{H},0} = 10^{21} \text{ cm}^{-2}$ and $\Sigma_{\text{CR},0} = 100 \text{ g cm}^{-2}$ is the cosmic ray attenuation depth (e.g., Umebayashi & Nakano 1980), above which we include an exponential truncation factor. We emphasize that this prescription is a rough heuristic, given the uncertainties associated with cosmic ray transport (see, e.g., recent work on modeling cosmic ray transport by Fitz Axen et al. 2024).

2.3 Thermodynamics

While the ISM is often assumed to be isothermal for simplicity, many important effects in star formation (such as the dynamics of fragmentation) require an explicit treatment of the thermal structure of the ISM (Lee et al. 2020). Therefore, for these calculations, we use a gas equation of state with a variable adiabatic index γ in order to account for variations in the ratio of para- to ortho-hydrogen, as well as the collisional dissociation of molecular H above $T \approx 2000$ K. The gas adiabatic index is calculated from a fit to density based on the results of Vaidya et al. (2015).

Since radiative processes are included, the numerical method must self-consistently co-evolve the gas, dust, and radiation field temperature, as in Hopkins et al. (2020). The numerical method operator-splits the adiabatic MHD evolution with a standard implicit cooling algorithm, which solves for equilibrium internal energy, temperature, net cooling/heating rate, mean molecular weight, and ionization state of the gas (treating the adiabatic heating rate from the MHD solver as an additional heating term; Hopkins 2017). Heating and cooling processes include molecular and fine-structure cooling, cosmic ray heating, dust cooling and heating, photoelectric heating (Draine 1978; Clark et al. 2012), metal line cooling, H photoionization, and collisional ionization of H and He. Details of the radiative cooling and thermochemistry modules are given in Hopkins et al. (2023). In addition to radiative feedback from sink particles (i.e., protostars/stars),

we include an external heating source at the boundary of the simulation domain that represents the interstellar radiation field (ISRF; assuming typical solar neighborhood conditions, Draine 2011).

2.4 Sink particles

Once dense cores undergo gravitational collapse to form protostars, these protostars begin injecting mass, momentum, and energy into their surroundings via a number of feedback mechanisms, such as radiation and collimated bipolar outflows (i.e., “jets”). In these simulations, the accretion, dynamics, and feedback of protostars and stars are modeled by using sink particles (e.g., Bate et al. 1995; Krumholz et al. 2004; Federrath et al. 2014; Hubber et al. 2013; Bleuler & Teyssier 2014), which are created on-the-fly from gas cells satisfying certain criteria (e.g., a density threshold, here $n_{\text{crit}} = 2 \times 10^{14} \text{ cm}^{-3}$). While the numerical scheme could continue to self-consistently follow collapse down to even higher densities, inserting sink particles at this point lowers the computational cost. At the current mass resolution $\Delta m = 10^{-5} M_{\odot}$, each sink particle represents an individual (proto)star.

The sink particle implementation presented in the STARFORGE framework allows gas cells to be accreted by a sink particle if they are within the sink particle radius (here $R_{\text{sink}} = 0.5 \text{ AU}$) and satisfy a number of boundedness/angular momentum/size/density criteria (see Grudić et al. 2021, for details). When a gas cell is accreted, the position, velocity, and internal angular momentum of the sink particle are updated to conserve center of mass, total momentum, and angular momentum.

The luminosity, temperature, and radius of each sink particle are evolved according to the sub-grid protostellar evolution prescription originally implemented in the ORION code by Offner et al. (2009). This model follows protostellar evolution through a sequence of phases, ending on the main sequence.

Sink particles act as radiation sources, injecting photons into five radiation bands (H ionizing, FUV, NUV, optical-NIR, and FIR) according to the spectral energy distribution set by the stellar evolution mode. To model radiative feedback, the radiation field is evolved in the five frequency bins using GIZMO’s M1 solver (Levermore 1984; Hopkins & Grudić 2019; Hopkins et al. 2020), in which gas cells exchange fluxes of radiation across effective faces (i.e., the same mesh-free volume discretization as used for MHD solver). Dust grains can scatter and absorb photons in all five bands, as well as radiate in the FIR band. Lyman continuum photons may be absorbed by HI. Absorbed ionizing photons are promptly re-radiated isotropically in the optical-NIR band; radiation absorbed in all other bands is re-radiated by dust in the FIR band.

As demonstrated by Offner & Chaban (2017); Guszejnov et al. (2021), protostellar jets are an important feedback mechanism and dramatically reduce stellar accretion rates. In calculations including sub-grid jet feedback, protostellar jets are modeled using the prescription of Cunningham et al. (2011): a fraction $f_w = 0.3$ of accreted material is launched along the sink angular momentum axis with speed $v_{\text{jet}} = f_K \sqrt{GM_*/R_*}$, with $f_K = 0.3$ (see Guszejnov et al. 2021, for a discussion on the effects of varying the parameters f_w and f_K on the IMF). Jets inject new gas cells (mass $\Delta m_w = 0.1 \Delta m$) in pairs near the sink particle, with opposite positions and velocities, conserving center of mass and momentum. Stellar winds and supernovae are also implemented in the numerical model, however these mechanisms are more relevant for high-mass star formation, and so are not included in our calculations of low-mass star formation.

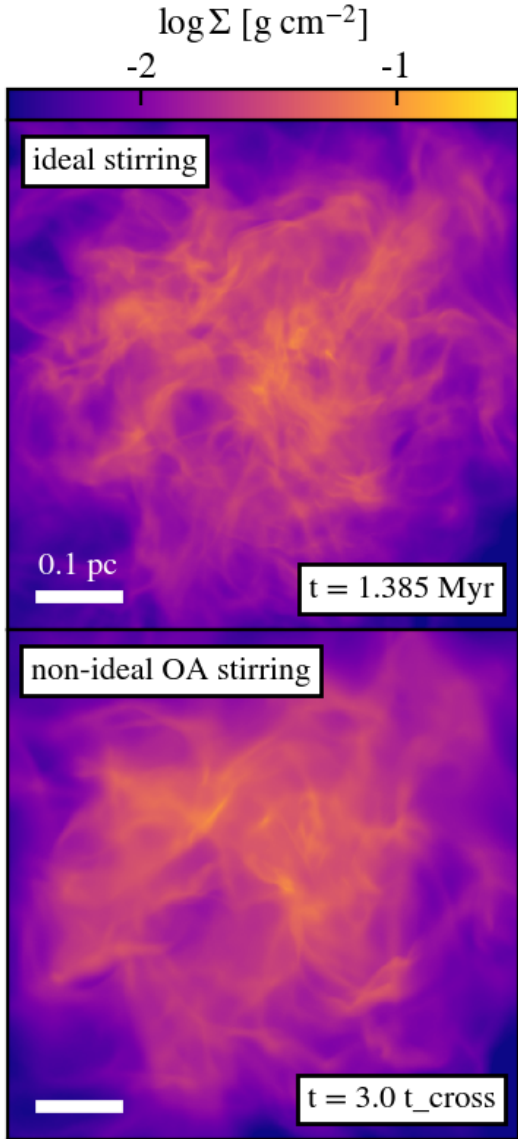


Figure 1. Projected column density at 3 turbulent crossing times ($t = 1.385$ Myr) during the TURBSPHERE stirring calculations. Top row: ideal MHD; bottom row: non-ideal Ohmic+AD.

3 RESULTS

We evolve the six models (three sets of MHD physics, with and without subgrid jet feedback), for approximately 2.5 – 3.5 free-fall times (1 – 1.4 Myr), until the gas in the vicinity of the star-forming region has largely been dispersed. Table 3 summarizes the protostar and protostellar disk formation outcomes for each model.

3.1 Cloud structure

We begin our comparison of the different models with a brief description of the global evolution, starting with the TURBSPHERE calculations and then proceeding to the star-forming calculations.

3.1.1 TURBSPHERE stirring calculations

To generate the initial conditions for the ideal and non-ideal MHD models, we evolve the TURBSPHERE stirring calculations for 3 turbulent crossing times ($t_{\text{cross}} = 0.465$ Myr) with two sets of MHD physics: ideal MHD and non-ideal MHD with Ohmic dissipation and ambipolar diffusion only.³ Figure 1 shows column density snapshots of the ideal and non-ideal models after 3 t_{cross} . As expected, the turbulent motions produce a non-homogeneous, filamentary structure. While the overall shape and structure of the cloud gas distributions are generally similar, owing to the use of the same initial turbulent seed, it is clear that the non-ideal model has fewer small-scale ($\lesssim 0.1$ pc) features. Small-scale structure is smoothed out and the densest structures appear broader and more massive with respect to the ideal MHD calculations. These results are generally consistent with previous non-ideal turbulent box calculations including ambipolar diffusion (e.g., Ntormousi et al. 2016, see discussion in Section 4.1).

3.1.2 Star-forming calculations

Figure 2 shows the gas column density of the ideal and two non-ideal (Ohmic+ambipolar, and Ohmic+ambipolar+Hall) MHD models just prior to the formation of the first sink particles (hereafter referred to as stars). The ideal model appears somewhat clumpier at small ($\lesssim 0.05$ pc) scales, possibly as a result of inheriting more small-scale structure from the initial conditions generated by the TURBSPHERE stirring phase. The non-ideal OA model appears to be the most smooth. The densest gas near the centers of the three models shows a variety of asymmetric structures, with a single dense core in the ideal model, and a number of cores connected by filamentary structures in the two non-ideal models. Figure 3 shows the effects of protostellar jet feedback on the global cloud morphology. The panels show the non-ideal OAH and non-ideal OAH+jets models at the same point in their evolution, after stars have formed. At this time, the jet bow shocks extend ~ 0.3 pc from the cloud center, with the ejected jet material forming thin, dense, elongated structures.

Figure 4 shows the magnetic field strength as a function of gas density for the three different sets of MHD physics just after the formation of the first stars. All three models show very similar levels of magnetization, with the magnetic field strength following $B \propto \rho^{1/2}$ between $\rho \gtrsim 10^{-21}$ and $\rho \lesssim 10^{-12} \text{ g cm}^{-3}$. This scaling with density is consistent with earlier studies (e.g., Mocz et al. 2017; Wurster et al. 2019; Guszejnov et al. 2022).

Figure 5 shows the values of the non-ideal MHD resistivities as a function of gas density in the non-ideal OAH model just after the formation of the first stars. As expected, ambipolar diffusion is most efficient and Ohmic resistivity is least efficient in the low-density gas (e.g., Mellon & Li 2009; Krasnopolsky et al. 2010; Wurster 2021). Ohmic resistivity becomes increasingly important as gas density increases. The Hall resistivity becomes the dominant non-ideal effect above $\rho \gtrsim 10^{-14} \text{ g cm}^{-3}$, and is negative throughout our parameter space. While the Hall resistivity may take either positive or negative values (e.g., Wardle & Ng 1999), the transition from negative η_H to positive η_H generally occurs at densities greater than $\rho \gtrsim 10^{-12} \text{ g cm}^{-3}$ for temperatures and magnetizations typical at this stage during the collapse (e.g., Wurster 2016).

³ To reduce the computational time, the Hall effect was not included in the non-ideal MHD stirring calculations. However, as ambipolar diffusion is expected to be the dominant non-ideal effect at the lower densities encountered during the stirring calculations, we do not expect these calculations to be substantially altered by the inclusion of the Hall effect.

Model protostar/protostellar disk formation summary				
Model label	MHD	Sub-grid jets	Num. protostars	Disk formation
ideal	ideal MHD	No	3	1 binary disk
ideal+jets	ideal MHD	Yes	4	1 quadruple disk
non-ideal OA	Ohmic+ambipolar	No	1	1 single disk
non-ideal OA+jets	Ohmic+ambipolar	Yes	5	2 single disks
non-ideal OAH	Ohmic+ambipolar+Hall	No	4	2 single → 2 binary disks
non-ideal OAH+jets	Ohmic+ambipolar+Hall	Yes	10	1 single → 1 binary disk

Table 4. Summary of included physics and description of protostar and protostellar disk formation outcomes for the six models.

3.2 Star formation outcomes

Figure 6 shows the mass evolution of all stars formed across all six models. Stars formed in models without jet feedback are shown as solid lines, while stars formed in models with jet feedback are shown as dashed lines. Star formation begins roughly $\sim 1\text{--}1.5 t_{\text{ff}}$ ($\sim 0.4\text{--}0.6$ Myr) after self-gravity is turned on and largely concludes within ~ 0.2 Myr, with the exception of the non-ideal OA+jets model, which experiences a second burst of star formation another ~ 0.2 Myr after the first two stars form. These secondary stars form from the fragmentation of a large rotating structure associated with the first stars (discussed further in Section 3.2.1). Star formation begins earliest in the two non-ideal OAH(+jets) models and latest in the two non-ideal OA(+jets) models. The total number of stars formed ranges from 1 (non-ideal OA) to 10 (non-ideal OAH+jets).

The calculations with sub-grid protostellar jet feedback are initialized from the final snapshots preceding star formation in the calculations with the same MHD physics but without jets, so all differences between the jet and no-jet models are due to jet feedback. We observe two clear trends once protostellar feedback is included. First, for each set of MHD physics, models with jets consistently form more stars than models without jets. Second, stars in models without jets are generally more massive, where the most massive stars in the models without jets are roughly an order of magnitude larger than those in the models with jet feedback. These trends are consistent with the radiation hydrodynamical studies of Hansen et al. (2012), who showed that jet feedback increased fragmentation and reduced the mass accretion rate. As discussed in Guszejnov et al. (2021), protostellar jets change the accretion history of stars not only by removing some fraction of the accreted gas to be ejected as jet feedback but also by disrupting the flow of gas around newly-formed stars.

3.2.1 Core/filament fragmentation and multiple system formation

We observe a variety of dense structures leading to star formation, which are broadly separable into two categories: (asymmetric) cores and filaments. Some multiple systems form from the fragmentation of a single core, such as the binary system in the ideal MHD model. Here, three stars form within ~ 6 kyr and $\sim 70\text{--}220$ AU of one another; the lowest-mass member of the triple is almost immediately ejected from the system. In other models, stars form from distinct cores, separated by $O(10\text{--}100)$ kyr in time and $O(10^3\text{--}10^4)$ AU in space, then migrate to become members of bound systems. Figure 7 shows stars forming like beads on a string along a filament in the two non-ideal OAH models at the same point in their evolution. The top row shows the model without jets, which has already formed its 4 total stars (these will later form two interacting binary systems); the bottom row shows the model with jet feedback, which has formed 6

out of its eventual 10 stars. This figure demonstrates the influence of jet feedback on gas density and structure and thereby the differences in fragmentation outcomes among the models. The jets themselves are not clearly visible in the surface density, although some bow shocks extending in the horizontal direction are visible in the bottom-left panel of Figure 7 and the gas distribution is somewhat more structured. The jets are clearly visible in the velocity dispersion shown in the bottom-right panel, however.

Figure 8 shows a rotating structure of radius ~ 2000 AU in the column density snapshots of the non-ideal OA+jets model just prior to the formation of the third star. A small over-density is visible in the structure, which becomes a star in the next snapshot. The fourth and fifth stars also form as this rotating structure fragments, likely due to gravitational instability. We note that this structure is not identified as a “disk” in our analysis, as the gas is below the $n > 10^9 \text{ cm}^{-3}$ density threshold used for disk identification (see Section 3.3.1 for the criteria used to define disks). Further analysis of this structure is presented in Appendix A.

3.3 Disk formation and evolution

We describe our criteria for identifying disks in our calculations and present an overview of the disks formed in our models. We then present the temporal evolution of bulk disk properties, degree of angular momentum alignment, and radial profiles.

3.3.1 Disk identification criteria

Following Joos et al. (2012), we identify disks based on a number of physically-motivated selection criteria:

- Disk material must be above a certain density threshold: $n > 10^9 \text{ cm}^{-3}$, where n is the number density;
- Disk material must be in Keplerian rotation and near hydrostatic equilibrium: $v_\phi > 2v_r$ and $v_\phi > 2v_z$, where v_r , v_ϕ , and v_z are the radial, vertical, and azimuthal velocities, with the rotation axis being the direction of the net angular momentum of the gas within ~ 6000 AU of the star(s) associated with the disk;
- Rotational support must exceed thermal support: $1/2\rho v_\phi^2 > 2P_{\text{th}}$, where ρ is the gas density and P_{th} is the thermal pressure; this check is intended to exclude the rotating central adiabatic core.

In each simulation snapshot, we first identify all disks associated with individual stars in order of least to most massive. We then identify all circumbinary disks associated with binary and higher-order systems. For “isolated” stars and stellar systems (i.e., separated from other stars by at least 6000 AU), we include all gas within a distance $r_{\text{max}} = 6000$ AU of the central star(s) when searching for disks. For stars with neighbors closer than 6000 AU, we set $r_{\text{max}} = 0.65r_{\text{nearest}}$, where r_{nearest} is the distance to the closest star or center of mass of

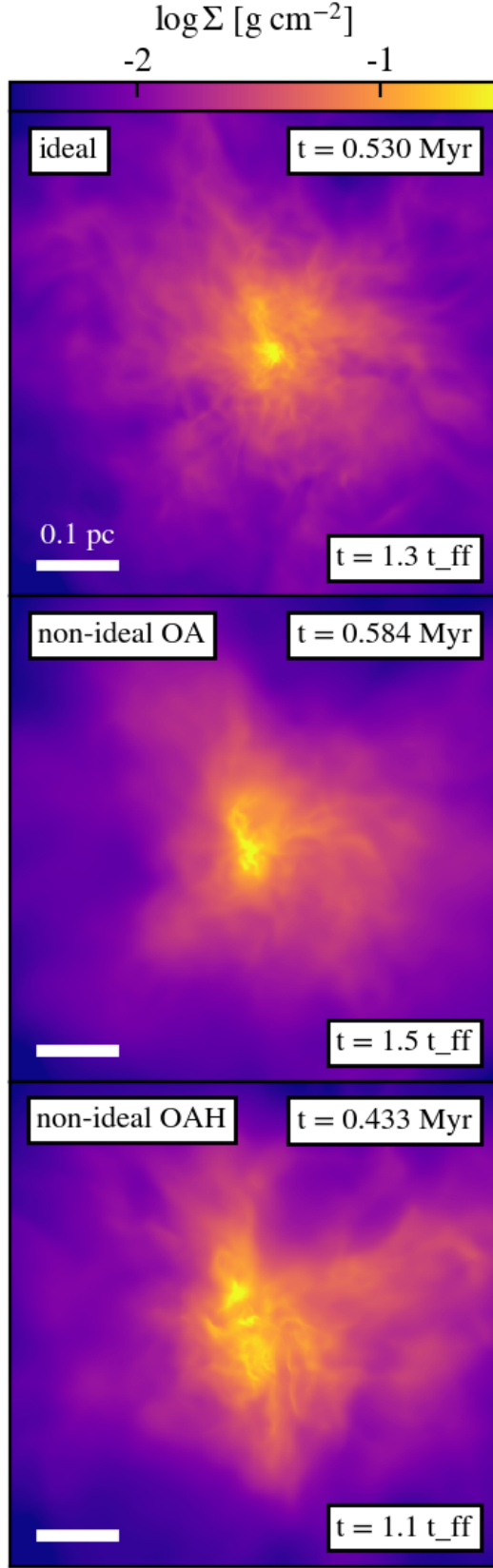


Figure 2. Projected column density just prior to the formation of the first sink particles (i.e., stars) for the different MHD models. Top row: ideal MHD; middle row: non-ideal Ohmic+AD; bottom row: non-ideal Ohmic+AD+Hall.

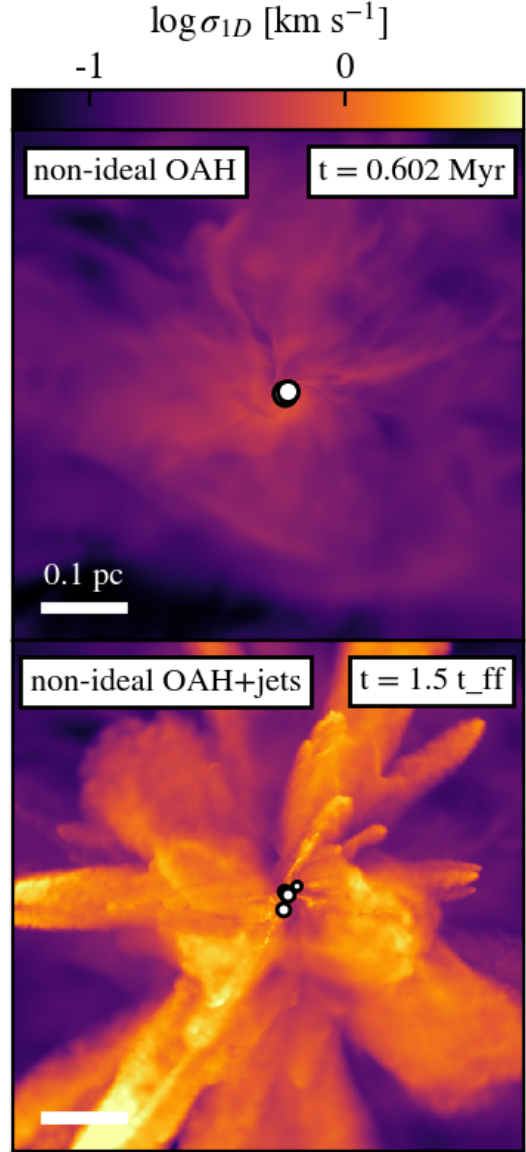


Figure 3. Line-of-sight 1D velocity dispersion (σ_{1D}) for the non-ideal OAH (top row) and the non-ideal OAH+jets (bottom row) models after stars begin to form, showing the effects of the sub-grid protostellar jet feedback on the global cloud morphology and kinematics. Markers indicate the positions of stars, with marker size proportional to stellar mass.

a bound stellar system; this prevents material visibly associated with a neighboring disk from being identified as disk material.

Most disks persist for several hundred kyr; however, a few transient disks appear for a snapshot or two (~ 6 – 12 kyr) before being disrupted by merging stellar systems and/or jet feedback from nearby stars; we exclude these short-lived disks from further analysis of the disk property evolution.

Using the above criteria, disks form in all of our models. However, the quadruple “disk” identified in the ideal+jets model is notably less massive ($M_{\text{disk}} \lesssim 10^{-3} M_{\odot}$) than the disks formed in the other models and contains less than 100 gas cells (often less than 10) in nearly all snapshots. We include this disk in our analysis of bulk disk properties, such as mass and radius, with the caveat that it is likely unresolved, but exclude it from more detailed analysis of disk radial

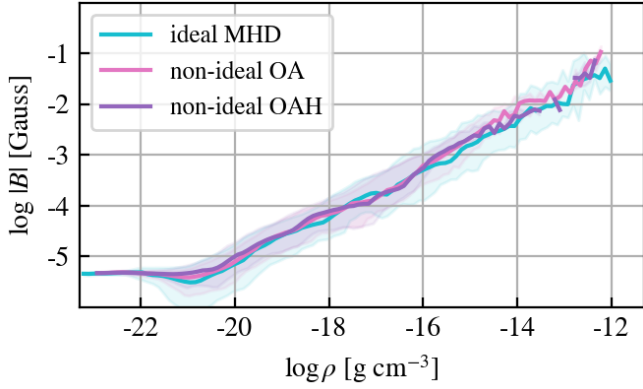


Figure 4. Magnetic field strength as a function of gas density for the ideal model (cyan) and two non-ideal MHD (pink: non-ideal OA; purple: non-ideal OAH) models just after star formation begins. The solid lines show the median value, while the shaded regions enclose the 5th and 95th percentiles.

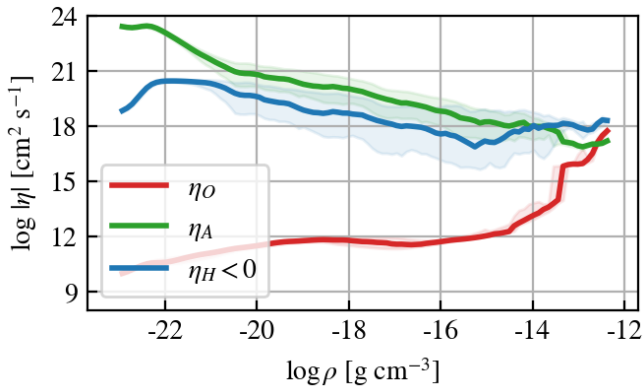


Figure 5. Non-ideal MHD resistivities as a function of gas density for the non-ideal OAH model just after star formation begins. The solid lines show the median value, while the shaded regions enclose the 5th and 95th percentiles.

structure in Section 3.3.6. Figure 9 shows the column density of this disk.

We observe a diverse set of disks and disk-hosting stellar systems. The non-ideal OA model forms a single massive star and hosts the most massive disk. The two single disks that form in the non-ideal OA+jets model exhibit the most variability in disk mass, possibly as a result of jet feedback from the secondary stars that form in the fragmenting rotating structure surrounding the first two stars, as seen in Figure 8. The non-ideal OAH model forms four stars, which become two interacting binary systems separated by ~ 1000 AU, as seen in Figure 10. The stellar masses are very similar, with the stars belonging to a given binary being closest in mass, and the circumbinary disk masses are also quite comparable. As seen in the figure, we observe a bridge of material connecting the two binary disks throughout their evolution. These two binary disks are fed material by two external arcing streams of material, which may be larger spiral arms or “streamers”, seen in observations as asymmetries in protostellar envelopes with total lengths ranging from ~ 500 AU to over 10^4 AU (Pineda et al. 2023). The non-ideal OAH+jets model forms a single disk at early times. This model forms the most stars and thus has the most chaotic, disruptive jet feedback during this period. A number of other circumstellar and circumbinary disks

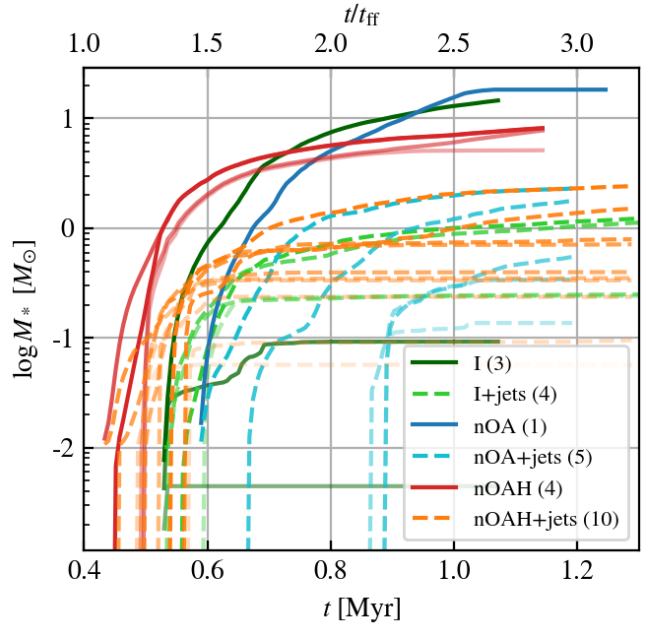


Figure 6. Mass evolution of stars formed in all models. The elapsed time is measured from the beginning of the star-forming calculations, e.g., after completion of the TURBSSPHERE stirring calculations.

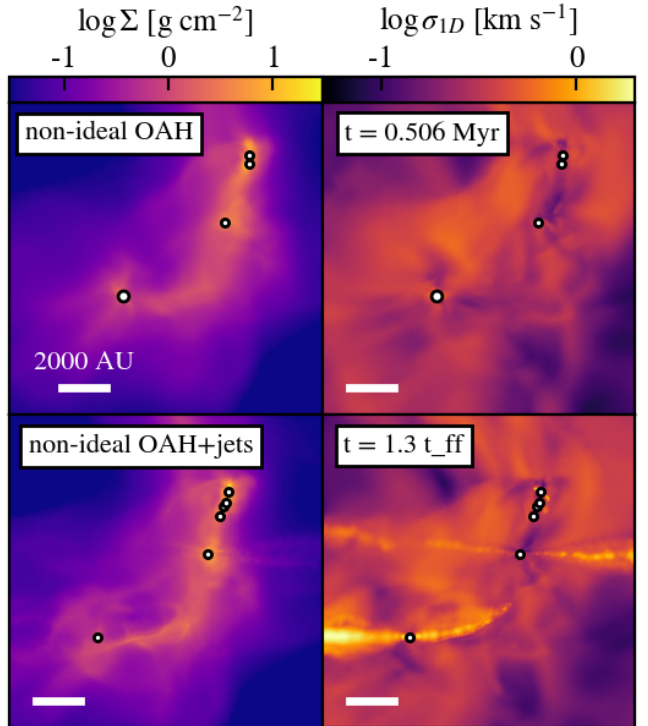


Figure 7. Column density (left column) and line-of-sight 1D velocity dispersion (right column) showing the formation of stars along a filament. Top row: non-ideal OAH; bottom row: non-ideal OAH+jets. Markers indicate the positions of stars, with marker size proportional to stellar mass.

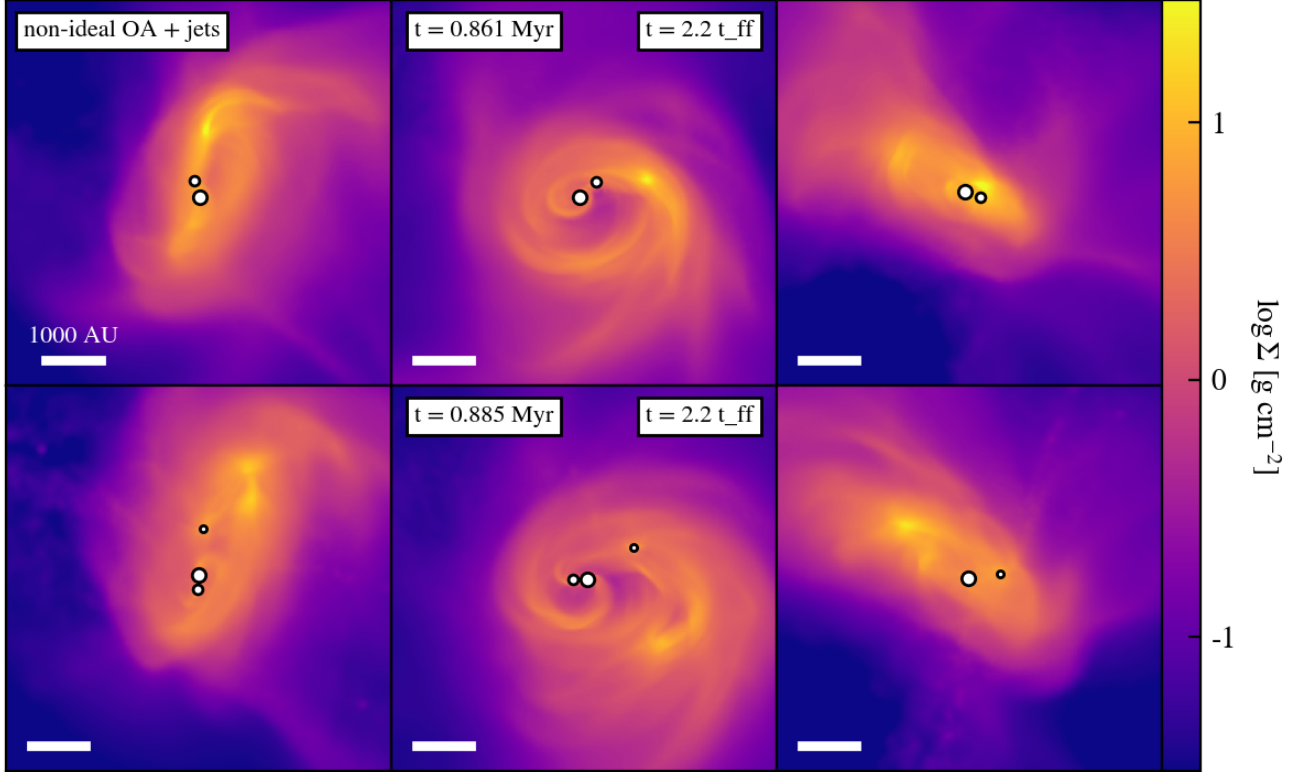


Figure 8. Column density projected along the x , y , and z -axes showing star formation in a rotating core of radius ~ 2000 AU. Top row: column density just prior to formation of third star. Bottom row: column density just prior to formation of fourth and fifth stars. Markers indicate the positions of stars, with marker size proportional to stellar mass.

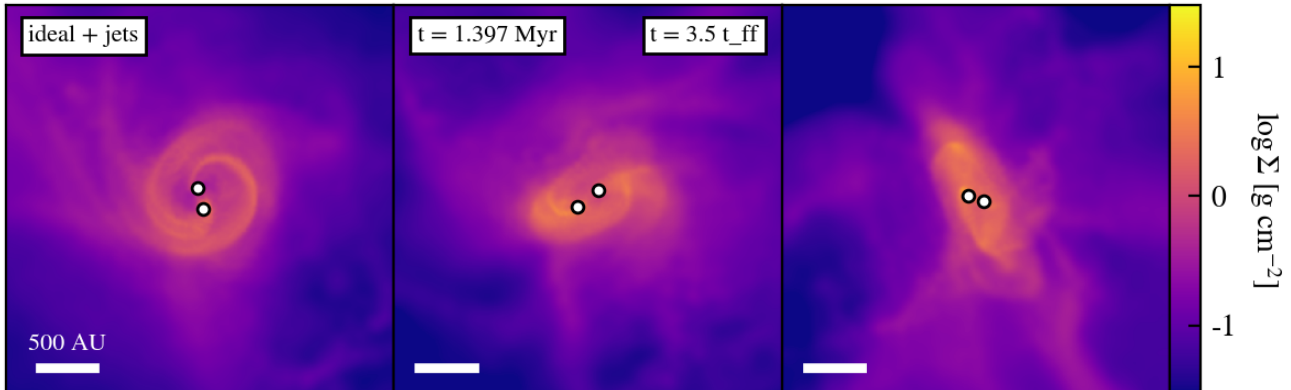


Figure 9. Column density projected along the x , y , and z -axes showing the low-mass quadruple disk that forms in the ideal+jets model. While only two markers representing stars are visible in each projection, there are four stars in two tight binaries in this quadruple system.

form during the first ~ 100 kyr following the onset star formation but persist for only a single snapshot or two before being disrupted by stellar interactions and jet feedback. However, about 200 kyr after the single disk disappears, a circumbinary disk forms and persists for at least another ~ 400 kyr. This binary system includes the star associated with the earlier single disk, and accretes material not from the natal core but from late-stage infalling gas.

3.3.2 Evolution of disk bulk properties

We examine the evolution of several bulk properties of the disks, such as the mass, radius, disk-to-stellar mass ratio, and aspect ratio.

We define the total disk mass to be the sum of the mass of all gas identified as belonging to the disk. Following Bate (2018), we then define the disk radius to be the radius containing 63.2 percent of the total mass. This is based on a truncated power-law surface density profile derived from models of viscously evolving disks (Lynden-Bell & Pringle 1974; Hartmann et al. 1998), often used to fit observed

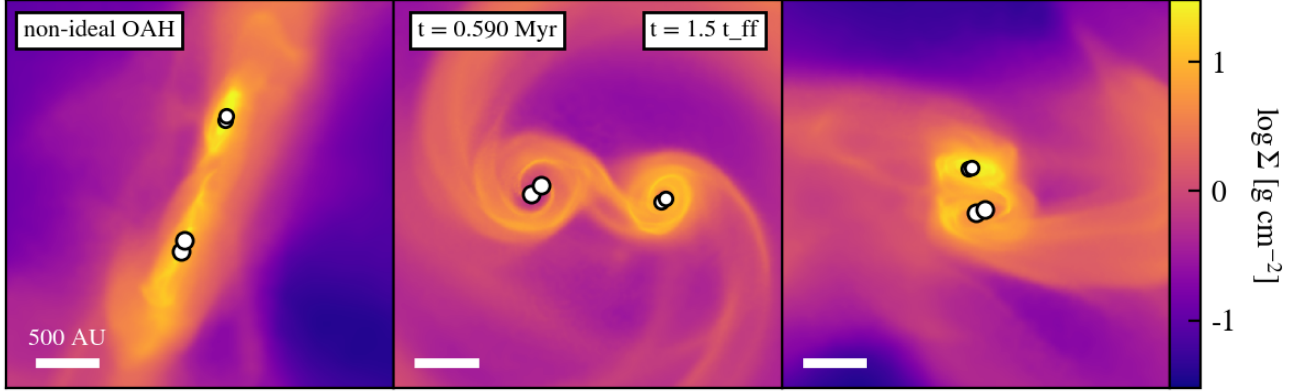


Figure 10. Column density projected along the x , y , and z -axes showing the two interacting binary systems that form in the non-ideal OAH model.

disks (e.g., Andrews et al. 2010; Tazzari et al. 2017):

$$\Sigma(r) = \Sigma_c \left(\frac{r}{r_c} \right)^{-\gamma} \exp \left[- \left(\frac{r}{r_c} \right)^{(2-\gamma)} \right], \quad (39)$$

where Σ_c is a normalization factor, r_c is the exponential cut-off radius, and γ is the power-law slope. Another approach defines the disk radius as the median value of the maximal disk extent in 50 equal-width azimuthal slices (see, e.g., Lebreuilly et al. 2024a). We find that both criteria give similar disk radii and so we adopt the criterion based on the total disk mass for our analysis.

Figure 11 and Figure 12 show the evolution of the disk masses and radii for all disks that persist for $\gtrsim 12$ kyr in all models; Figure 13 shows the evolution of the disk-to-stellar-mass ratio. We find that most disks form within ~ 100 kyr of the formation of the host stars (see the dashed lines representing stellar masses in Figure 11) and then persist for ~ 100 –300 kyr. The disks are typically most massive soon after formation and become less massive with time. Disk radii range from a few 10 to a few 100 AU, broadly consistent with observations of circumstellar and circumbinary disks (see discussion in Section 4.3). The disk-to-stellar mass ratio decreases with time but initially exceeds $M_{\text{disk}}/M_{\text{star}} \gtrsim 0.1$ for several disks. No disk fragmentation is observed (see also Section 3.3.5).

To compute the disk aspect ratio, we center the coordinates of all disk cells about the disk center of mass, compute the covariance matrix of the centered coordinates, and obtain the eigenvalues λ_j of the covariance matrix. The disk aspect ratio is then defined to be $q = \min_j(\sqrt{\lambda_j})/\max_j(\sqrt{\lambda_j})$. Figure 14 shows the evolution of the aspect ratio of all disks persisting for $\gtrsim 12$ kyr. We see that most of the disks have an aspect ratio $q \lesssim 0.2$ for most of their evolution, and that the aspect ratio tends to decrease with disk age.

We note that the variability in the disk masses and radii is physical and not simply due to statistical fluctuations in the number of included cells. Disk morphologies visibly vary over multiple timesteps, and fluctuations in disk masses closely follow changes to the disk specific angular momentum. Disk masses and radii at early times (e.g., during the Class 0/I phases) are controlled by the infalling angular momentum from the envelope and/or feeding filaments, and as it is not guaranteed that the angular momentum vector of the infalling material will remain constant, it is likely that disk sizes do not grow monotonically with time (see, e.g., the review by Kratter & Lodato 2016).

3.3.3 Angular momentum and magnetic field misalignment

Figure 15 shows the relative angle between the sink particle and disk specific angular momentum vectors⁴, used as a proxy for the disk and stellar rotation axes, where for circumbinary disks, we use the angular momentum vector of the most massive star associated with the disk. We see that the angular momentum vectors tend to be generally well-aligned ($\theta_{\text{rel}} \lesssim 20$ degrees) for most of the disk evolution. Several disks are initially quite misaligned with their stars ($\theta_{\text{rel}} \sim 60$ –80 degrees), and then become more aligned with time; this is expected as disks continue to transfer angular momentum to the central star(s).

Figure 16 shows the evolution of the angle between the disk angular momentum vector and the direction of the mean local magnetic field, where the mean local magnetic field is the field averaged over a 1000 AU sphere centered at the disk center of mass. The disks formed in the models with non-ideal MHD including only Ohmic dissipation and ambipolar diffusion show a tendency for alignment perpendicular to the local magnetic field, albeit with some significant variability ($\sim \pm 60^\circ$). The long-lived binary disks formed in the non-ideal MHD models with the Hall effect included, meanwhile, show a tendency for increasing misalignment with the local magnetic field, reaching angles $\gtrsim 150^\circ$.

We note that most of the variability in Figure 16 is due to changes in the orientation of the local magnetic field; the disk angular momentum vector changes orientation on much longer timescales.

3.3.4 Which stars host disks?

Disks form in all models, but not all stars are associated with disks. Figure 17 again shows the mass evolution of all stars across all models but now emphasizing the stars hosting disks. We see that, by the end of the simulation, the stars with disks are consistently the most massive stars in that model. The smallest stars, meanwhile, are typically either components of close binaries or else are dynamically ejected into the low-density gas, where there is little material available for disk formation. It is also possible that these stars host disks that fall below

⁴ The sink particle angular momentum includes the angular momentum of all gas cells accreted by the sink particle. The sink particle angular momentum is not, strictly speaking, the same as the stellar angular momentum as there are unresolved processes which may affect the angular momentum transport between the gas and the star; however, it represents our best estimate of the stellar angular momentum direction.

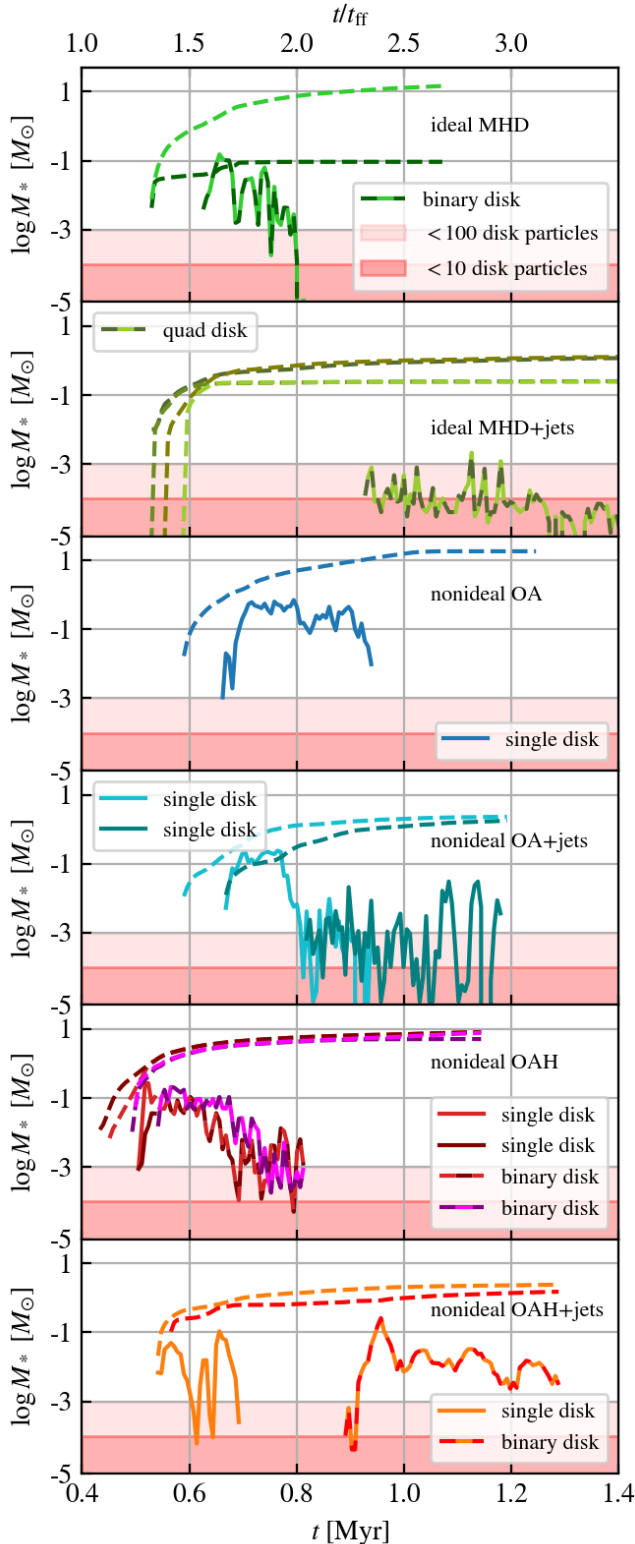


Figure 11. Disk mass evolution. The elapsed time is measured from the beginning of the star-forming calculations (when self-gravity is enabled). The dotted lines show the masses of the stars associated with each disk. Dashed lines combining multiple colors represent circumbinary disks. Disks persisting for less than ~ 12 kyr are not depicted. Red shaded regions indicate when disks contain less than 100 gas cells and may be poorly resolved.

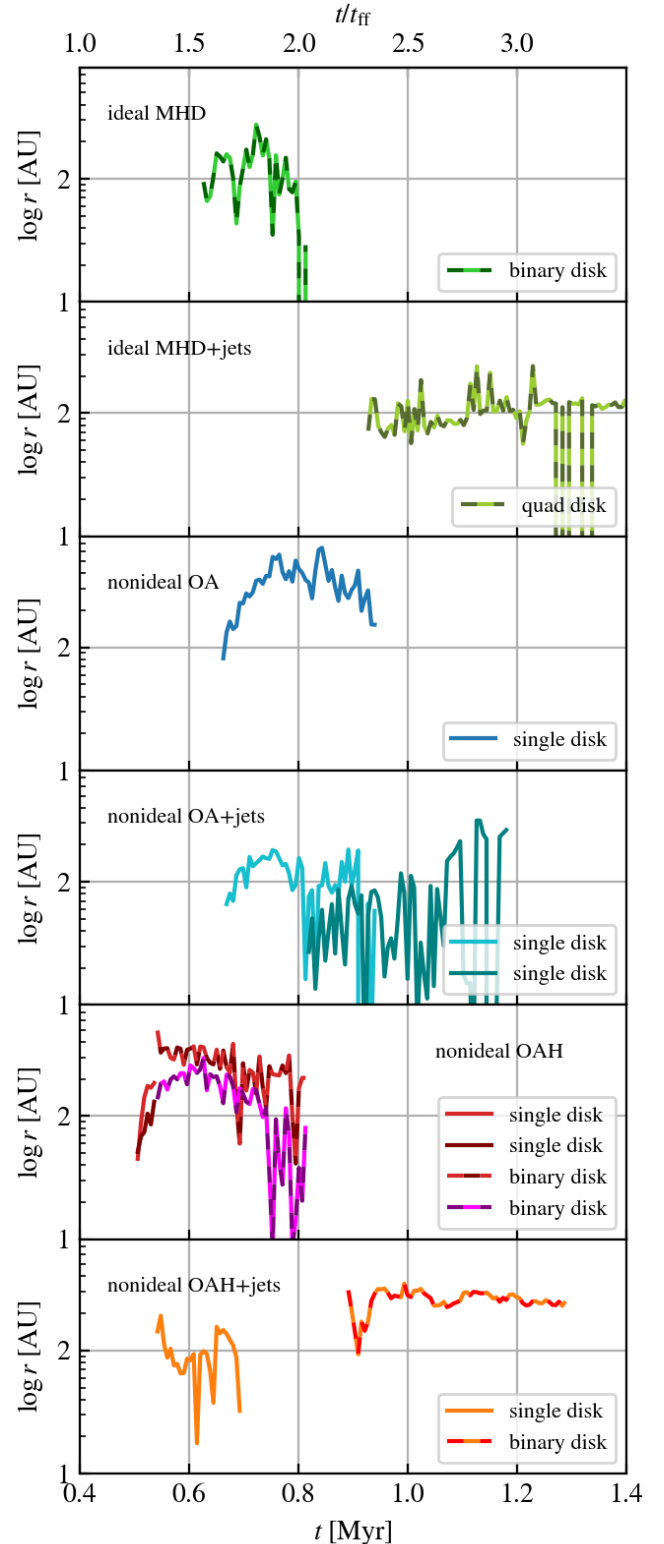


Figure 12. Same as Fig. 11, but showing the evolution of the disk radius, taken to be the radius containing 63.2 percent of the total disk mass.

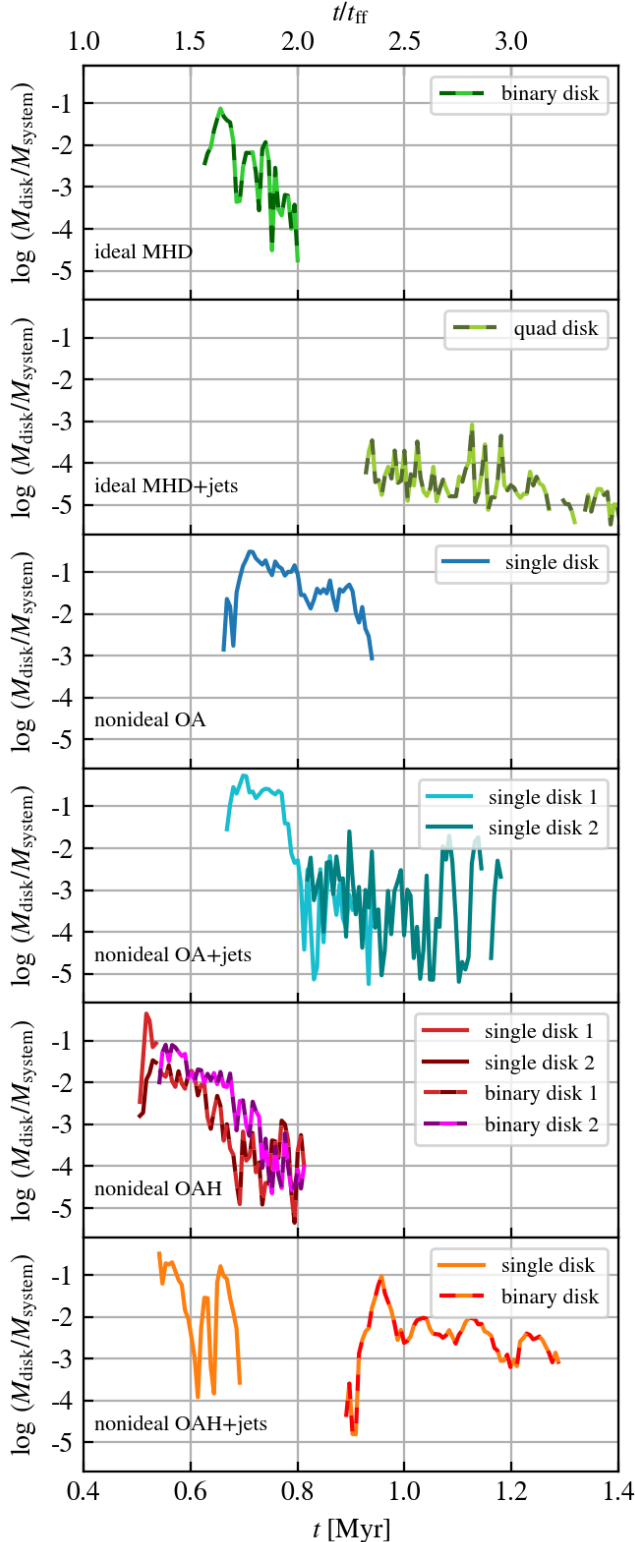


Figure 13. Same as Fig. 11, but showing the evolution of the ratio of disk to stellar mass.

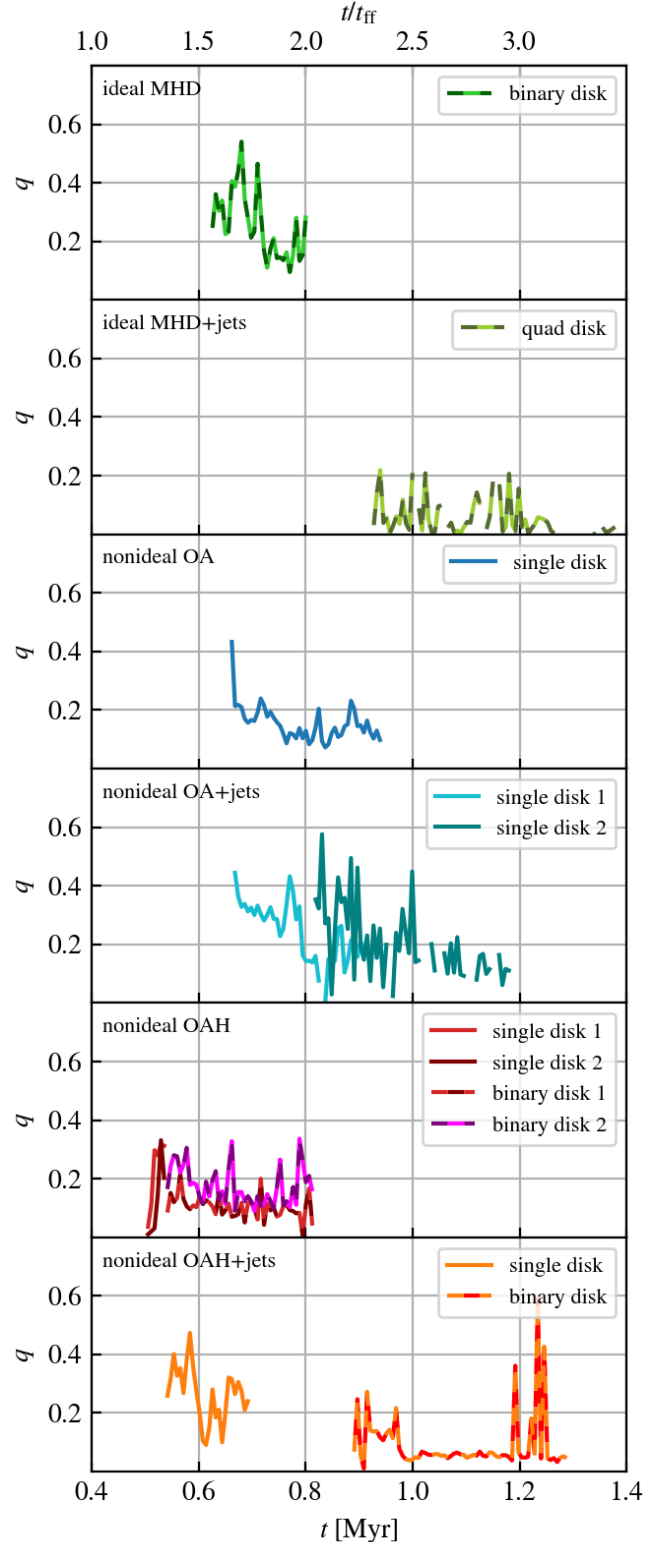


Figure 14. Same as Fig. 11 but showing the evolution of the disk aspect ratio.

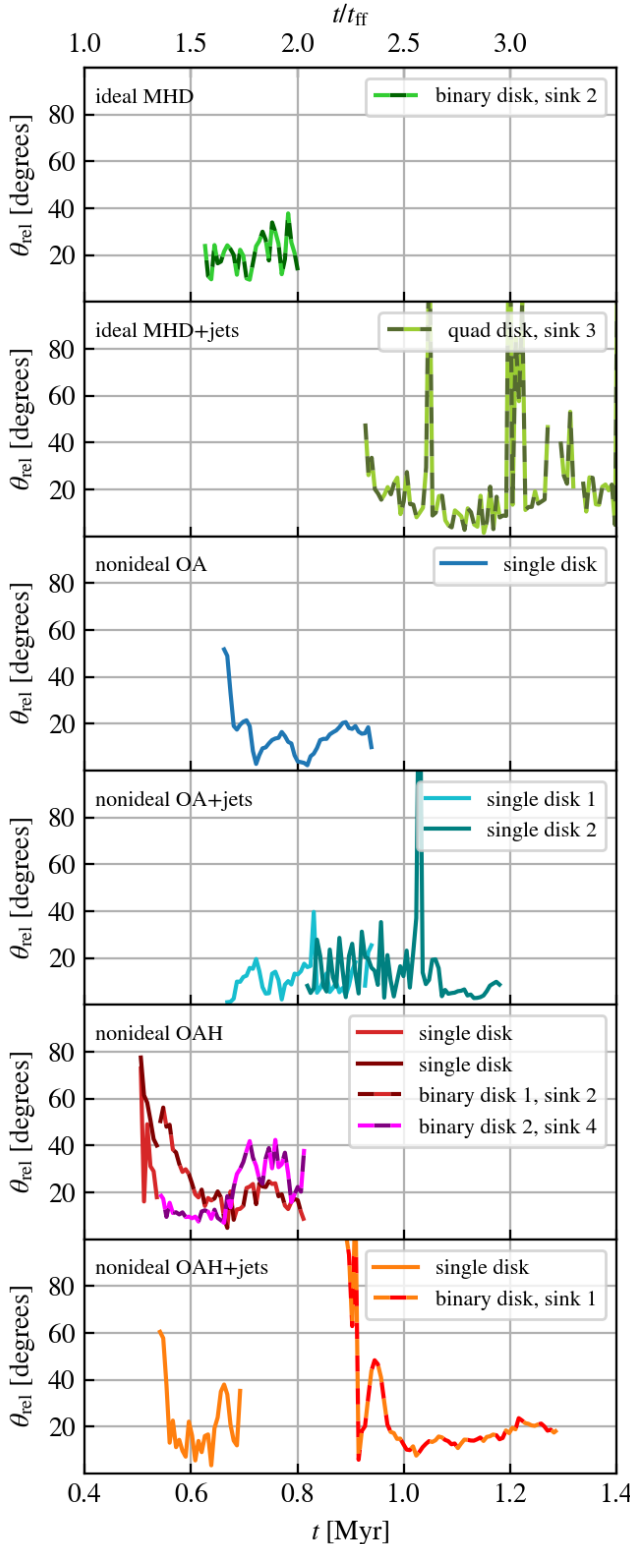


Figure 15. Evolution of the misalignment angle between the disk and sink particle specific angular momentum vectors, where for multiple systems we consider only the angular momentum of the most massive sink particle. The sink particle angular momentum vector is not quite the same as the stellar angular momentum vector due to unresolved processes but represents our best available estimate.

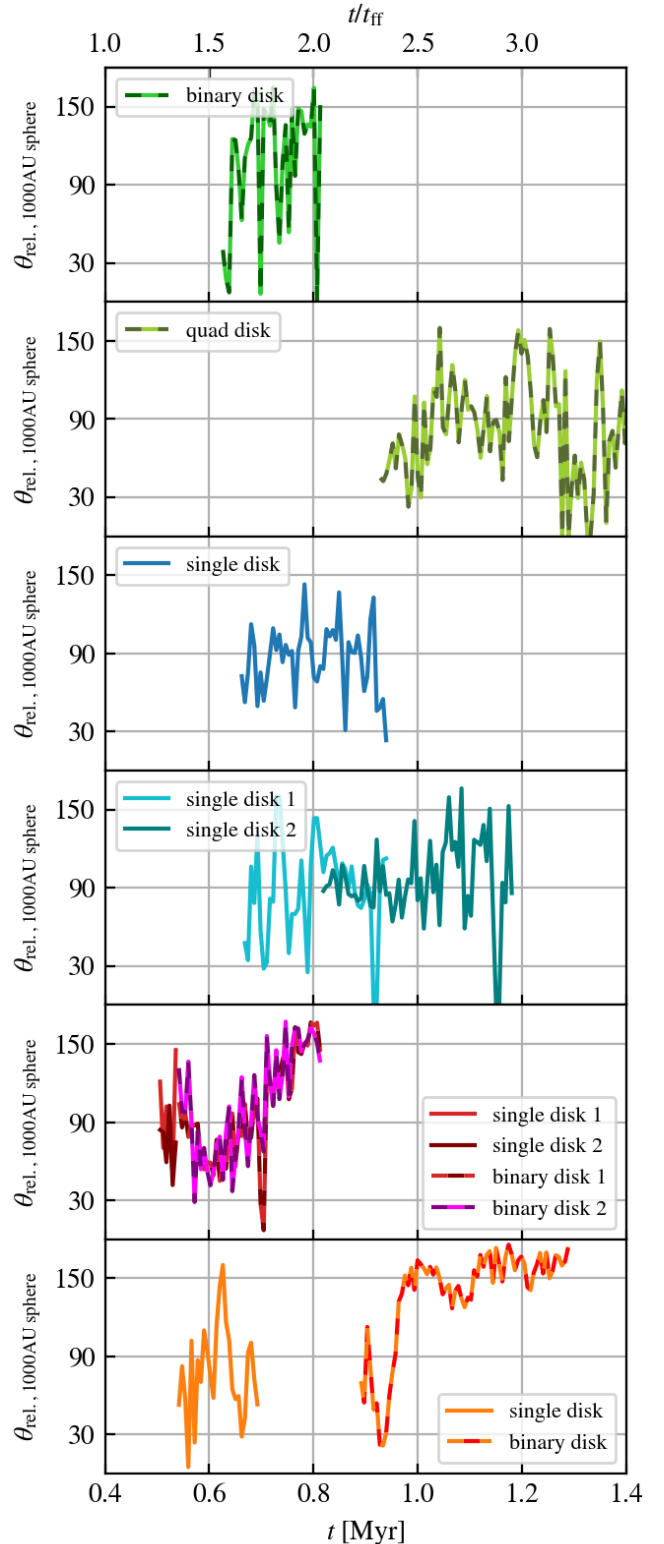


Figure 16. Evolution of the misalignment angle between the disk angular momentum vector and the mean local magnetic field direction for all disks formed. The mean local magnetic field is averaged over all gas within a 1000 AU radius centered at the disk center of mass.

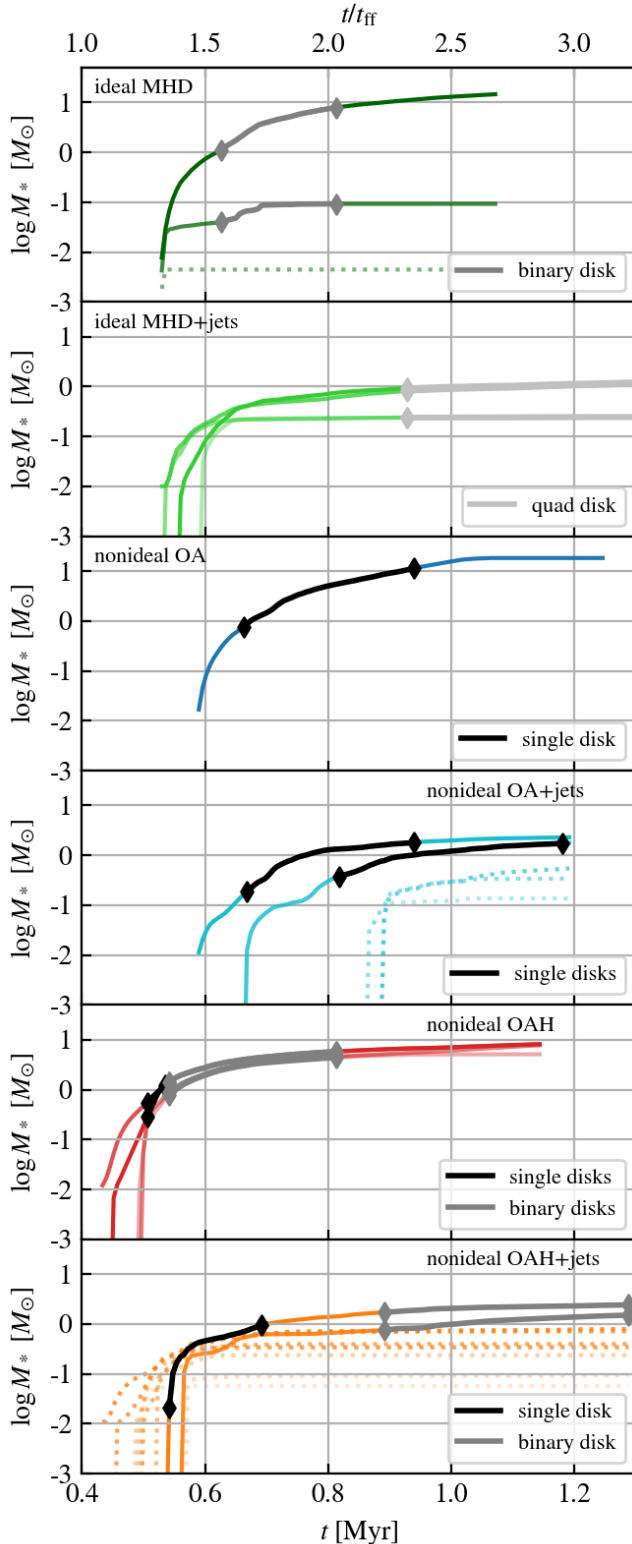


Figure 17. Mass evolution of all stars in all models, highlighting disk presence. Solid colored lines correspond to stars associated with a disk at some point during the calculations; dotted lines correspond to stars with no disks. Black and gray line sections indicate the presence of disks. Diamond markers indicate the first and last snapshots in which a given disk exists.

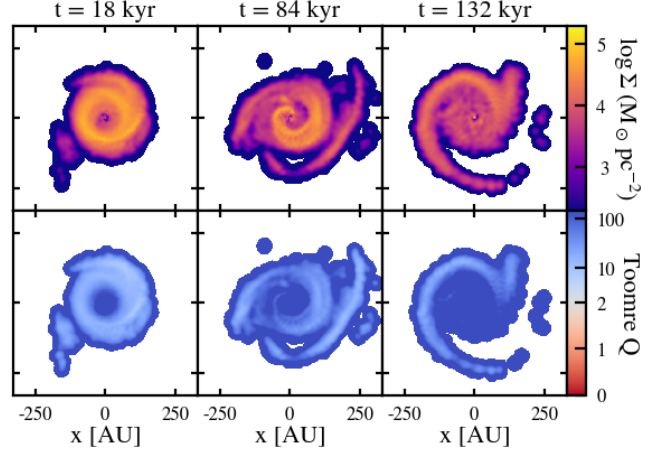


Figure 18. Projected surface density (top row) and Toomre Q (bottom row) for the binary disk formed in the ideal MHD model. We project along the direction of the net angular momentum of the gas, and use a linear colormap normalization between $Q = 0$ and $Q = 2$ and a logarithmic normalization for $Q > 2$.

our disk mass criterion (i.e., more than 100 gas cells belonging to the disk, or $M_{\text{disk}} \geq 0.001 M_{\odot}$).

The disk lifetimes, ranging from $\lesssim 200$ to $\gtrsim 400$ kyr, are consistent with estimated Class 0/I lifetimes, during which protostars are embedded in their natal envelopes (Dunham et al. 2014).

3.3.5 Disk stability

A protostellar disk may become gravitationally unstable and fragment to form companion stars and/or planets. The standard reference for estimating the onset of gravitational instability in differentially-rotating, self-gravitating disks is the Toomre Q parameter (Toomre 1964):

$$Q = \frac{c_s \kappa}{\pi G \Sigma}, \quad (40)$$

where c_s is the sound speed, κ the epicyclic frequency (equal to the angular velocity in a Keplerian disk), G the gravitational constant, and Σ the surface density. The disk is stable against fragmentation for $Q > 1$. As $Q \rightarrow 1$, self-gravity becomes increasingly important and the disk becomes unstable due to the growth of spiral density waves.

We calculate the Toomre Q for the disks formed in our models and find that the disks are generally stable against gravitational fragmentation. Figure 18 shows the evolution of Q for the binary disk formed in the ideal MHD model, where $Q \gg 1$ throughout the disk lifetime. Figure 19 shows the evolution of Q for the single disk formed in the non-ideal OA model, which forms the most massive disk. This disk has regions where $1 \lesssim Q \lesssim 2$, corresponding to marginal gravitational instability and the development of spiral waves. We observe no disk fragmentation in any of our models (though see Appendix A for further discussion of the rotating fragmenting envelope in the non-ideal OA+jets model).

3.3.6 Disk radial profiles

In addition to examining the evolution of bulk disk properties such as mass and radius, we also construct radial profiles of disk properties

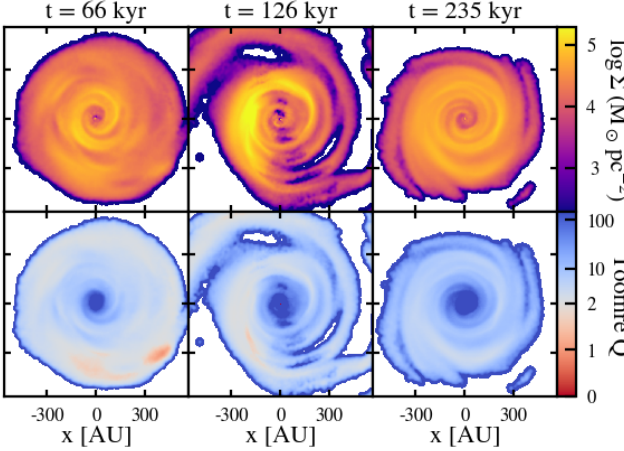


Figure 19. Projected surface density (top row) and Toomre Q (bottom row) for the single disk formed in the nonideal OA MHD model.

such as density, magnetic field strength, angular velocity, temperature, and nonideal resistivities. We create the radial profiles by sorting the gas cells belonging to each disk by distance to the disk center of mass, binning the cells into 50 bins containing approximately equal cell counts, and taking the average value of each bin. For each disk, we plot the radial profile for each snapshot in which the disk contains at least 1000 cells (i.e., $M_{\text{disk}} \geq 0.01 M_{\odot}$).

Figure 20 shows the evolution of the radial density profiles. It is not clear whether a power-law of the form $\rho(r) \propto r^a$ can be used to characterize the density profile of the disks, owing to the presence of density structures (such as spirals), observed as peaks and valleys in the density profiles. The density generally decreases in time as the disk becomes less massive. For binary disks, the inner cavity observed in the radial profiles tends to correspond with the binary separation: the binary in the ideal MHD model (first row, first column of the figure) and the second binary in the non-ideal OAH model (first row, fourth column) are close binaries with separation $\lesssim 10$ AU, while the first binary in the non-ideal OAH model (first row, third column) and the binary in the non-ideal OAH+jets model (second row, fourth column) are separated by ~ 100 AU.

Figure 21 shows the evolution of the radial profiles of the disk magnetic field strength, which generally follow a $B(r) \propto r^{-1}$ relation. The magnetic field strength in the ideal MHD disk is comparable to that in the non-ideal MHD models. In some disks, such as the single disk in the non-ideal OA model (first row, second column), the magnetic field strength increases with time; in other disks, such as the binary disk in the non-ideal OAH+jets model (second row, fourth column), the field strength decreases with time.

As seen in Figure 22, the angular velocity profile of each disk shows clear Keplerian rotation, $\omega(r) \propto r^{-3/2}$, with the angular velocity increasing with time as the disk continues accreting material and angular momentum. It appears that gravitational torques (seen as spiral structures) and magnetic braking are somewhat inefficient at transporting angular momentum on disk scales.

Figure 23 shows the evolution of the radial temperature profiles. In general, the disk is heated by stellar irradiation, which acts at the disk surface, and viscous dissipation due to accretion, which is maximal at the disk midplane (Ueda et al. 2023). The disk temperature structure is therefore a function of the vertical coordinate z as well as the radial coordinate r , and depends on the optical properties of the disk. A simplified model for disk midplane temperature is (e.g., Sierra &

Lizano 2020; Ueda et al. 2023)

$$T_{\text{disk}} = \left(T_{\text{irr}}^4 + T_{\text{acc}}^4 \right)^{1/4}, \quad (41)$$

where T_{irr} and T_{acc} denote the disk temperature determined by stellar irradiation and accretion heating, respectively. For a passively-heated, flared disk in radiative equilibrium, the temperature due to stellar irradiation can be estimated as (e.g., Chiang & Goldreich 1997; Dullemond et al. 2001; Huang et al. 2018)

$$T_{\text{irr}}(r) = \left(\frac{\varphi L_*}{8\pi\sigma_{SB}r^2} \right)^{1/4} \propto r^{-1/2}, \quad (42)$$

where φ is the flaring angle of the disk ($\varphi \ll 1$), L_* the stellar luminosity, and σ_{SB} the Stefan-Boltzmann constant. The temperature due to viscous heating during accretion, meanwhile, can be approximated as (e.g., Nakamoto & Nakagawa 1994; Sierra & Lizano 2020)

$$T_{\text{acc}}(r) = \frac{3}{4} \left(\tau_R + \frac{2}{3} \right) \frac{3\dot{M}\Omega_K}{8\pi\sigma_{SB}} \propto r^{-3/4}, \quad (43)$$

where τ_R is the Rosseland optical depth measured perpendicular to the disk midplane, \dot{M} the accretion rate, and $\Omega_K = \sqrt{GM_*/r^3}$ the Keplerian angular velocity for stellar mass M_* . We show both $T(r) \propto r^{-3/4}$ (accretion-dominated heating) and $T(r) \propto r^{-1/2}$ (irradiation-dominated heating) as solid black lines in the top-left panel of Figure 23. Viscous heating is expected to dominate at early times and small radii, while heating by stellar irradiation is expected to dominate at larger radii and during later stages of disk evolution (e.g., Ueda et al. 2023). For most disks in our models, $T(r) \propto r^{-3/4}$ appears to be a better fit to the disk radial profiles, consistent with expectations of accretion-dominated heating. However, when we examine the radial temperature profiles of all gas contained within spheres of radius $\sim 10^5$ AU centered at the disk center of mass, we observe a better fit to $T(r) \propto r^{-1/2}$ for gas beyond a few 100 AU of the center, suggesting that stellar irradiation dominates the heating in this region.

Figures 24, 25, and 26 show the evolution of the radial profiles of the Ohmic dissipation, ambipolar diffusion, and Hall effect resistivities throughout the disks. Ohmic resistivity is most efficient in the inner disk ($r \lesssim 100$ AU), with a steep drop-off in the outer regions of the disk, but is subdominant to both ambipolar diffusion and the Hall effect. Ambipolar diffusion is more efficient in the outer disk. In models including the Hall effect, the Hall effect generally dominates over ambipolar diffusion and Ohmic resistivity throughout most of the disk. We do not observe a clear systematic trend with time in any of the non-ideal MHD resistivities, which are complex, non-linear functions of the gas density, temperature, magnetic field strength, and properties of charged species (see Eq. 6). For example, as seen in the top two panels of Figure 26, the Hall resistivity throughout the two binary disks in the non-ideal OAH model fluctuates over a range of values with no clear time dependence; however in the non-ideal OAH+jets model, the Hall resistivity increases with disk age for the single disk, but decreases with disk age for the binary disk, as seen in the bottom two panels of Figure 26.

3.4 Self-consistent outflows

Although we include a model with sub-grid protostellar jet feedback for each set of MHD physics in our calculations, we also observe some self-consistently launched outflows in our ideal MHD model with no sub-grid jet feedback. Figure 27 shows the time evolution of this outflow as seen in the column density when projected along the

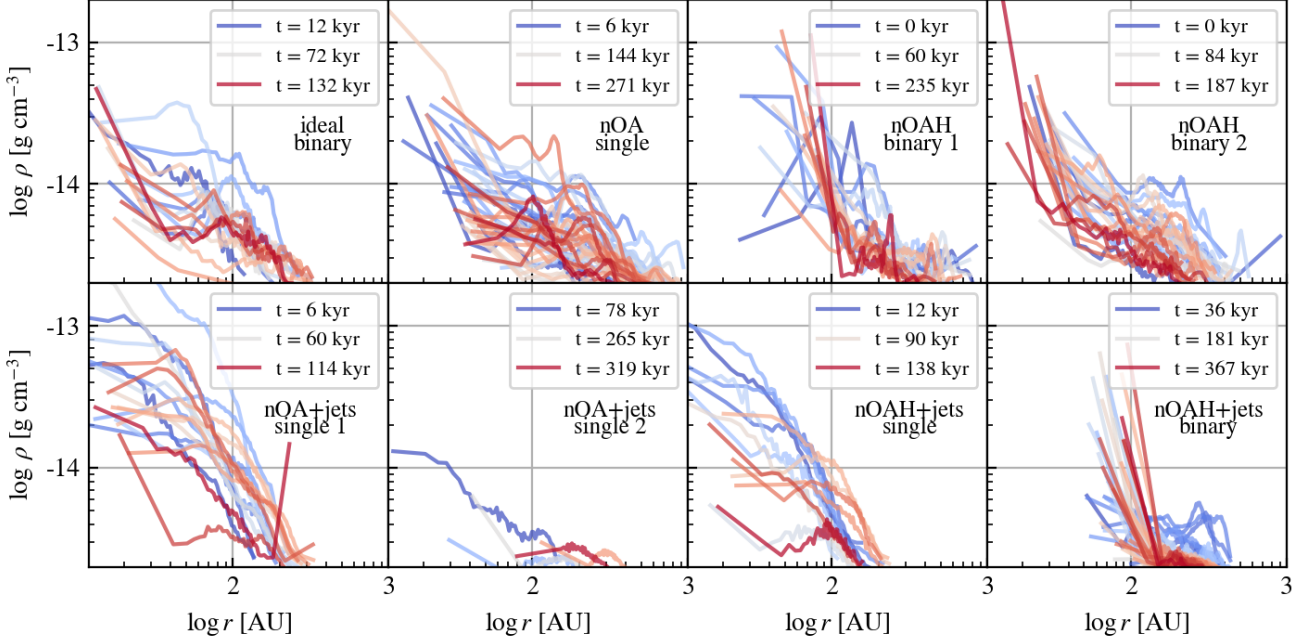


Figure 20. Time evolution of the radial density profiles of all disks formed across all models. Only snapshots with disks containing ≥ 1000 gas cells are plotted. Blue lines correspond to earlier snapshots; red lines correspond to later snapshots.

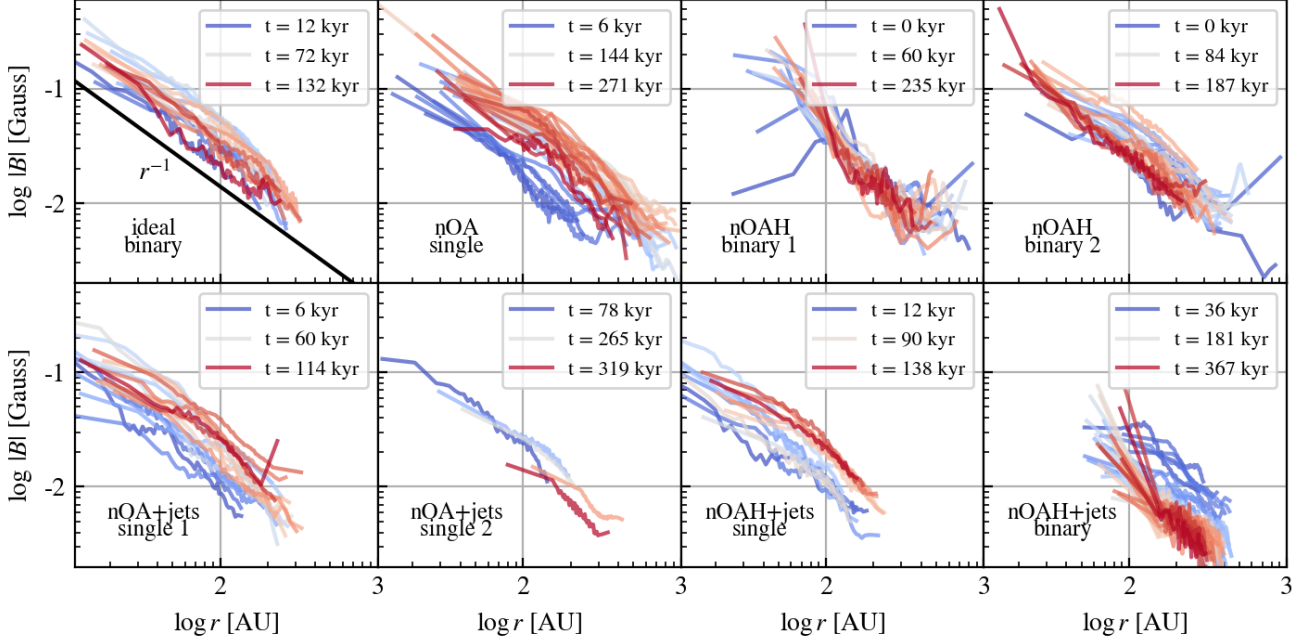


Figure 21. Same as Figure 20 but showing radial profiles of the magnetic field strength.

x-axis. The outflow is launched from the central binary disk system and is approximately parallel to the plot *x*-axis. A bow shock due to the outflow can be seen in the figure. We note, however, that this outflow is less collimated and has significantly lower velocity than the sub-grid jet feedback. Figure 28 shows the 1D line-of-sight velocity dispersion σ_{1D} of this outflow in the top panel; for comparison, the bottom panel shows the velocity dispersion of the ideal+jets model at the same point in time. The left lobe of the outflow can be distinguished in the top panel of Figure 28. While the sub-grid jets approach a velocity dispersion of $\sigma_{1D} \sim 10 \text{ km s}^{-1}$, the self-

consistent outflow in the top model is closer to $\sigma_{1D} \sim 0.5 \text{ km s}^{-1}$, more than an order of magnitude lower. We observe no self-consistent outflows in any of the non-ideal MHD models.

4 DISCUSSION

We have presented the results of a suite of six calculations following the formation of stellar clusters and protostellar disks under various assumptions of ideal and non-ideal MHD and with optional sub-

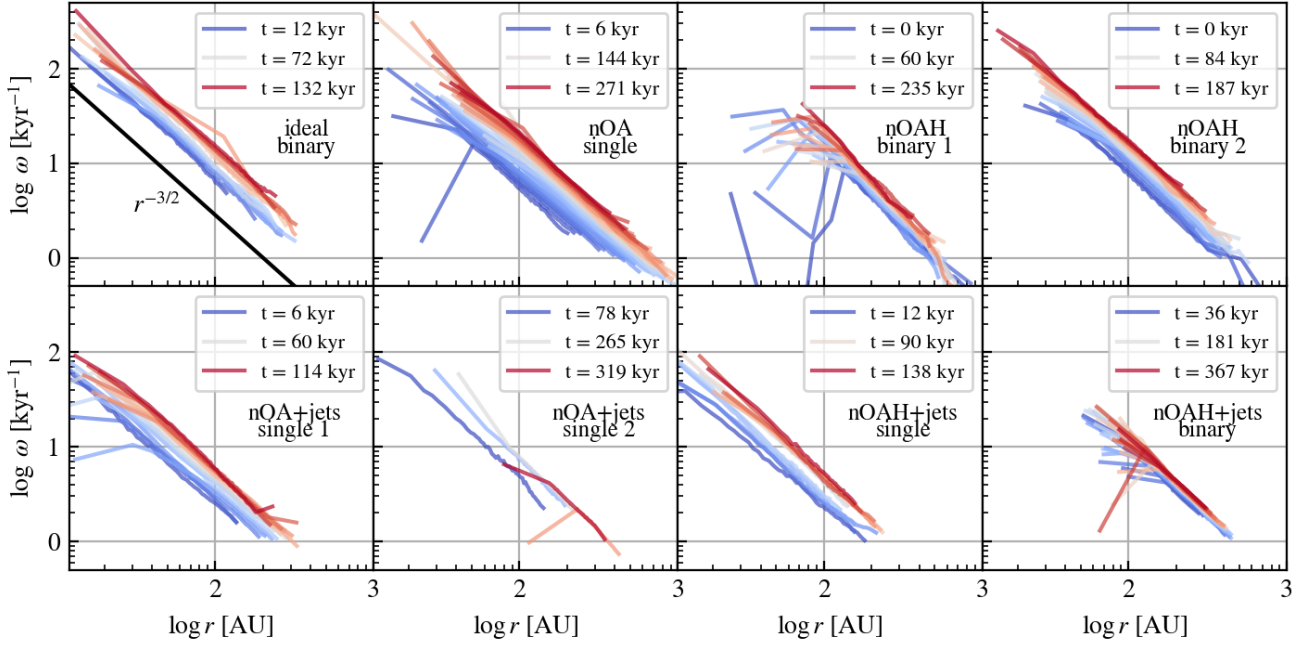


Figure 22. Same as Figure 20, but showing radial profiles of the angular velocity.

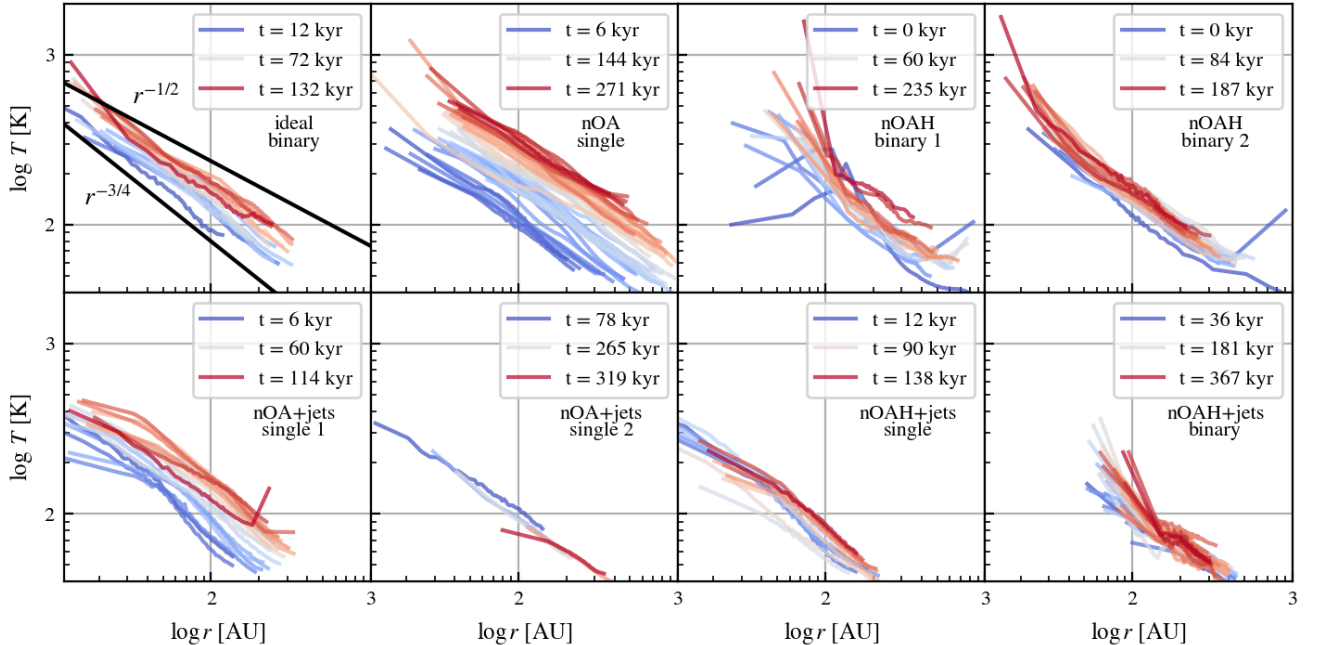


Figure 23. Same as Figure 20, but showing radial profiles of the gas temperature.

grid protostellar jet feedback. Here, we discuss differences in stellar and disk formation outcomes among our models and compare our results to several previous numerical studies. We also discuss several challenges which complicate drawing direct comparisons between observed and modeled disk properties, before concluding with a few caveats concerning the validity of our microphysical model used to calculate the non-ideal MHD resistivities.

4.1 Effects of including non-ideal MHD

Prior to initiating the self-gravitating star-forming calculations, we observe smoother cloud structure in the calculations with non-ideal (Ohmic+ambipolar) MHD than in the ideal MHD calculations. This is consistent with the turbulent box calculations of [Ntormousi et al. \(2016\)](#), who compared the effects of assuming ideal MHD vs. including ambipolar diffusion. As molecular clouds consist of a low ionization plasma dominated by neutral species, ion-neutral friction has been invoked as a damping mechanism for interstellar turbulence, leading to a cutoff in the turbulent energy cascade below a charac-

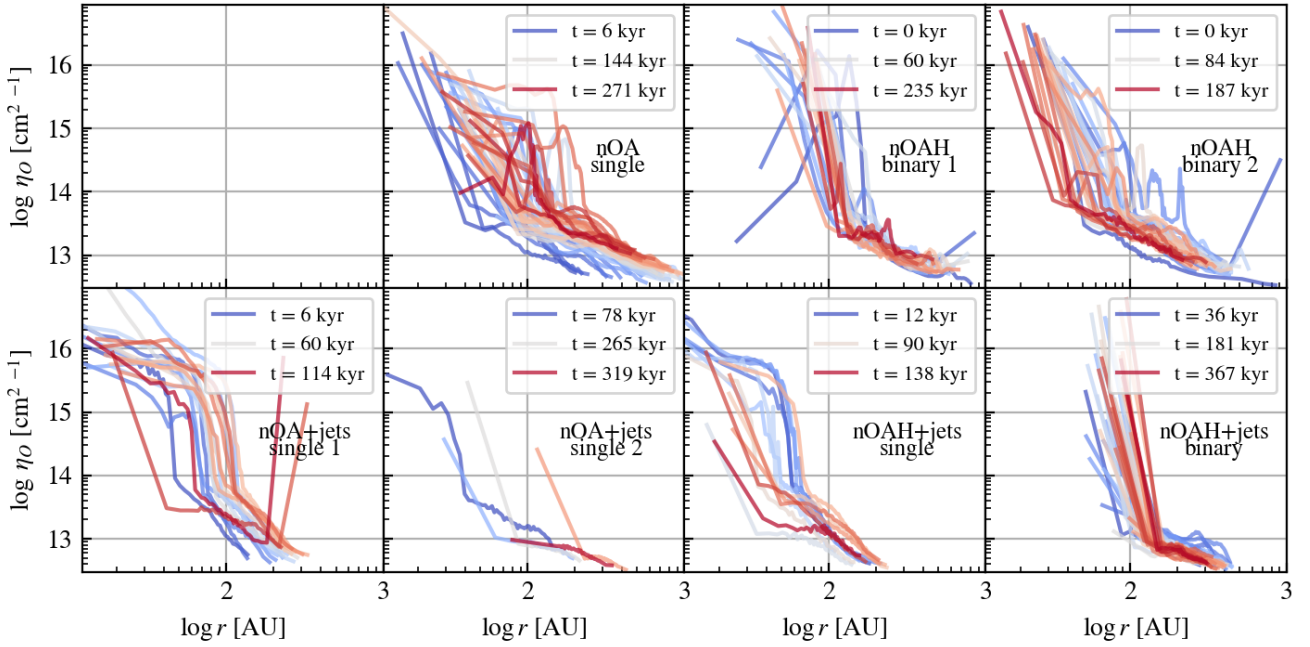


Figure 24. Same as Figure 20, but showing radial profiles of the Ohmic dissipation resistivity, η_O .

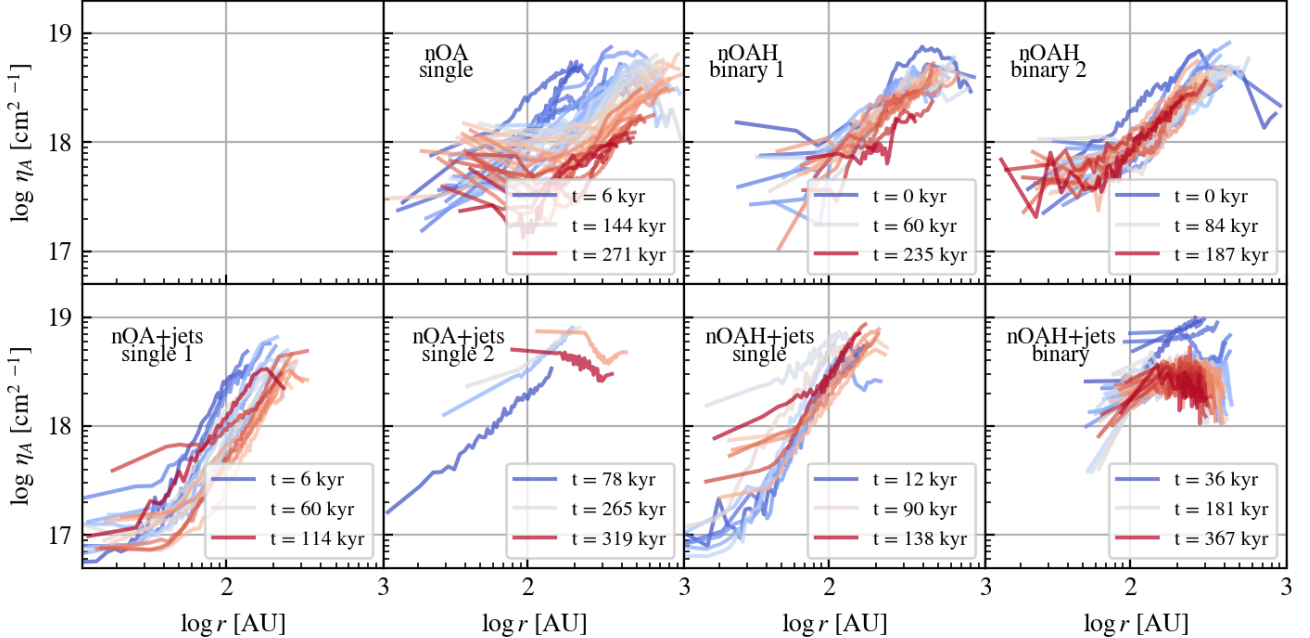


Figure 25. Same as Figure 20, but showing radial profiles of the ambipolar diffusion resistivity, η_A .

teristic ambipolar diffusion length scale at which the motions of the two species decouple (Zweibel & Josafatsson 1983; Mouschovias 1991; Brandenburg & Zweibel 1994; Li & Houde 2008). Ntormousi et al. (2016) found that the density and magnetic field morphologies differed between the two sets of MHD physics, with the densest structures becoming broader and more massive under the influence of ambipolar diffusion. We note that several other studies of cluster formation with non-ideal MHD, such as Wurster et al. (2019) and Lebreuilly et al. (2024a), found that the evolution of the large-scale structure ($\gtrsim 0.05$ pc) is independent of whether ideal or non-ideal

MHD is assumed. These studies, however, do not include an initial turbulent stirring phase equivalent to our TURBS SPHERE calculations. We also note that recent observations of the nearby star-forming region NGC 1333 by Pineda et al. (2024) found no evidence of dissipation in both the ion and neutral power spectra down to ~ 4000 AU scales, suggesting that the characteristic ambipolar length scale, if it exists, is below this scale.

We continue to observe differences in structure once self-gravity is turned on and star formation begins. Figure 2 shows that, just prior to star formation, the ideal MHD model is the most structured, and the

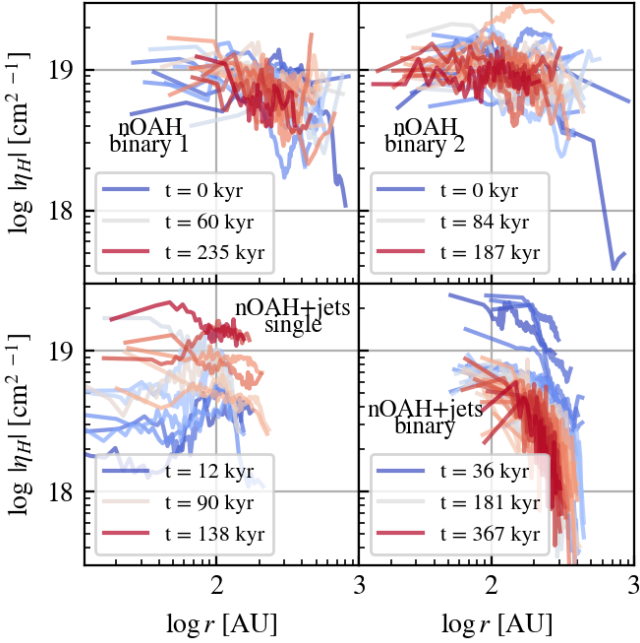


Figure 26. Same as Figure 20, but showing radial profiles of the absolute value of the Hall effect resistivity, $|\eta_H|$.

densest region is more centrally concentrated. The morphology of the dense gas also differs between the two non-ideal MHD models, which can be attributed to inclusion of the Hall effect. Ambipolar diffusion tends to relax magnetic field bending via the magnetic tension force, acting in the same direction as the bending of the field lines. The Hall effect, meanwhile, induces a Hall drift orthogonal to the magnetic field bending and is not in principle a diffusive term. These two terms may induce fluid motions orthogonal to one another (see, e.g., Zhao et al. 2021), resulting in different density and magnetic field structures. The onset of star formation, as well as the number of stars formed, differs between the models, likely as a result of these structural differences.

In almost all of our models, disks form shortly (~ 100 – 200 kyr) after the onset of star formation, as seen in Figure 17, and persist another ~ 100 – 300 kyr. Contrary to the “magnetic braking catastrophe”, disk formation occurs even in the ideal MHD models. However, the quadruple “disk” in the ideal+jets model is notably less massive than the disks formed in other models and is not well resolved given our mass resolution of $\Delta m = 10^{-5} M_\odot$. As a binary disk forms in the ideal MHD model with no jets, it is possible that our sub-grid jet feedback model, and not the ideal MHD assumption, is more disruptive to disk formation. Aside from the quadruple “disk” in the ideal+jets model, we observe no significant differences in disk properties such as mass, radius, or magnetization between the binary disk in the ideal MHD model and the disks in the non-ideal MHD models. We caution, however, that our sample of disks is too small to draw any conclusions about disk population statistics. Further studies beginning with a larger initial cloud mass and forming a greater number of disks are necessary to make any definitive statements about differences in disk properties between ideal and non-ideal MHD models.

Our disk formation outcomes are in agreement with the study of low-mass cluster formation by Wurster et al. (2019), who concluded that “there is no magnetic braking catastrophe.” They modeled the collapse of $M_0 = 50 M_\odot$ turbulent molecular cloud cores using

smoothed particle hydrodynamics (SPH) calculations containing $N = 5 \times 10^6$ particles (i.e., using the same mass resolution $\Delta m = 10^{-5} M_\odot$ as in our calculations) and including radiative transfer and all three non-ideal MHD effects. They compared the results of assuming ideal vs. non-ideal MHD as well as varying the initial mass-to-magnetic flux ratio $\mu_\Phi = 3, 5, 10$, and 20 . Their models formed 8–19 stars by $1.45 t_{\text{ff}} (275.5 \text{ kyr})$, likely due to their higher initial cloud density $\rho_0 = 1.22 \times 10^{-19} \text{ g cm}^{-3}$ compared to our $\rho_0 = 2.77 \times 10^{-20} \text{ g cm}^{-3}$. They found that single disks of radii ~ 10 – 80 AU and multiple disks of radii up to ~ 500 AU formed in all of their models, with no obvious dependence on model parameters. The magnetic field strength in the disks was independent of the initial magnetic field strength of the cloud, although the disk field strengths in the non-ideal MHD models spanned a narrower range of values, suggesting that non-ideal MHD processes may moderate the disk magnetic field. These calculations did not include protostellar feedback.

As the Hall effect is numerically challenging to implement, several works investigating non-ideal MHD in stellar cluster and protostellar disk formation have focused on ambipolar diffusion only. Our non-ideal OA and non-ideal OA+jets models can be directly compared with these works. Lebreuilly et al. (2024a) calculated the collapse of $M_0 = 500$ – $1000 M_\odot$ molecular clouds with radiative transfer and ambipolar diffusion using adaptive mesh refinement (AMR), investigating the effects of ideal MHD vs. ambipolar diffusion, varying the initial mass-to-magnetic flux ratio, and using flux-limited diffusion vs. assuming a barotropic equation of state. Their fiducial non-ideal MHD model, which was integrated up to a final star formation efficiency (SFE) of 0.15 , had $\mu_\Phi = 10$ and formed 88 stars, with approximately 70% of stellar systems hosting a disk at some point during the calculations. They compared disk properties at birth, 10, and 20 kyr after formation; we note that this is a significantly earlier stage of disk evolution than is reached in our models. They found that the initial mass-to-magnetic flux ratio ($\mu_\Phi = 10, 50$) had a greater effect on disk size and radius than including ambipolar diffusion, with typical disk sizes of ~ 30 – 40 AU in the $\mu_\Phi = 10$ models and ~ 60 – 80 AU in the $\mu_\Phi = 50$ models.

In addition to non-ideal MHD effects, misalignment between the magnetic field direction and initial rotation axis of the cloud has been investigated as a possible resolution to the magnetic braking catastrophe. The isolated spherical collapse, $M_0 = 1 M_\odot$ ideal MHD calculations of Joos et al. (2012) found that massive disks formed in all of their models with an initial misalignment $\theta_B \gtrsim 20^\circ$ and mass-to-flux ratio $\mu_\Phi \gtrsim 2$. The resistive (i.e., Ohmic) non-ideal MHD calculations of Machida et al. (2020) showed that the disk, outflow, and magnetic field axis are rarely aligned, except when $\theta_B = 0^\circ$, and that outflows tend to be suppressed when $\theta_B = 90^\circ$. Most of the disks in our model show some tendency to be perpendicular to the local magnetic field, albeit with significant scatter, as seen in Figure 16. The disks in the Hall models, however, become increasingly anti-aligned with the local field over time. This is consistent with the 2D axisymmetric calculations of Zhao et al. (2021), who found that disks formed during Hall-dominated collapse could only have an anti-aligned magnetic field polarity, such that $\omega_{\text{disk}} \cdot \mathbf{B} < 0$. Again, a larger statistical sample is needed in order to make any definitive statements on the impact of non-ideal effects on disk orientation.

4.2 Effects of including protostellar jet feedback

Our models with jet feedback consistently show increased fragmentation when compared to their counterparts with no feedback, resulting in more stars being formed, as summarized in Table 3. The final masses of the stars formed in models with jets are also roughly

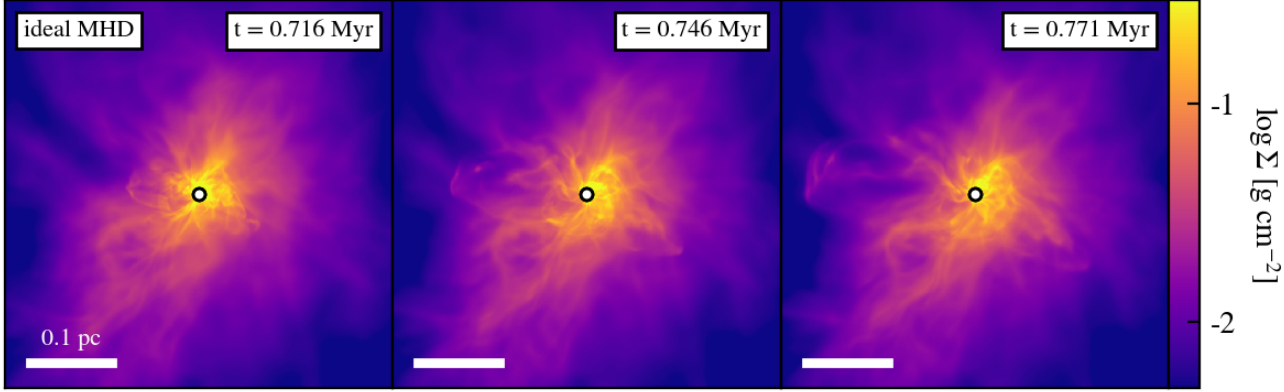


Figure 27. Column density projected along the x -axis showing the time evolution of the self-consistently launched outflow in the ideal MHD model. The outflow is launched from the central binary and is nearly parallel to the plot x -axis in this projection.

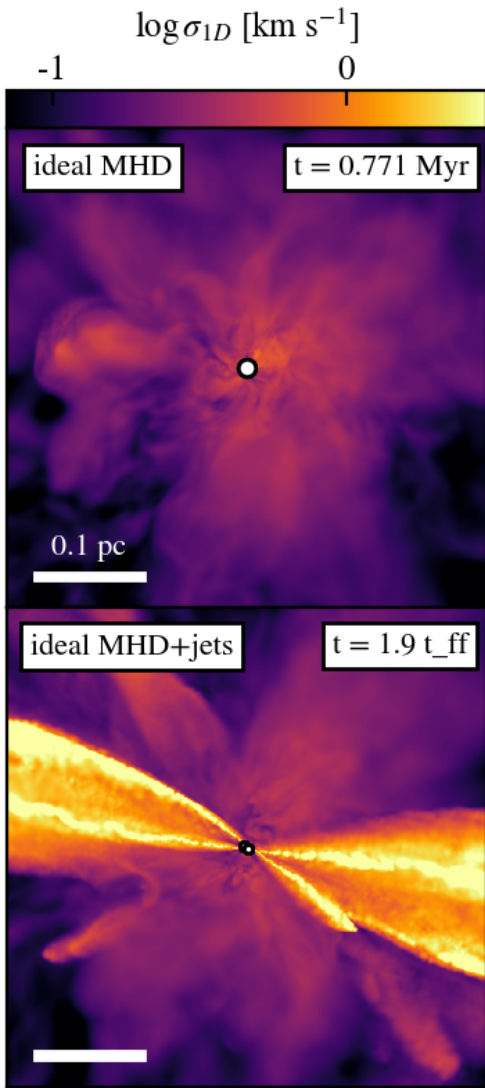


Figure 28. Line-of-sight 1D velocity dispersion (σ_{1D}) along the x -axis for the ideal MHD (top row) and the ideal+jets (bottom row). The top panel shows the same time and viewing angle as the rightmost panel of the projected column density plot in Figure 27.

an order of magnitude less massive than those formed in models without jets, as seen in Figure 6. Previous calculations examining the effects of including protostellar feedback, such as radiation and jets, on low-mass star formation by Hansen et al. (2012), showed that while radiative feedback can suppress fragmentation, outflows reduce protostellar masses and accretion rates and thereby luminosities. When outflows are included, the total stellar luminosity drops by an order of magnitude and radiation is much less effective at suppressing radiation. Calculations by Guszejnov et al. (2021) using the STARFORGE numerical framework also showed that including jet feedback dramatically disrupts the accretion flow on < 0.1 pc scales and shifts the turnover in the stellar initial mass function (IMF) to smaller scales.

We observe disk formation in our models both with and without jet feedback, although it is possible that our jet feedback prescription is somewhat disruptive to disk formation, particularly when there are many nearby stars. The non-ideal OAH+jets model, which forms 10 stars within a ~ 120 kyr period, only forms one disk which persists for longer than a couple of snapshots ($\gtrsim 18$ kyr): a number of other disks formed at this time are destroyed by jet feedback from neighboring protostars a snapshot or two ($\sim 6-12$ kyr) after formation. The ideal+jets model, meanwhile, forms the smallest and least-resolved quadruple “disk” out of all models.

As discussed in Section 3.4 and shown in Figure 27, we observe a loosely-collimated, low-velocity ($\sigma_{1D} \sim 0.5$ km s $^{-1}$) outflow ejected from the binary disk system in the ideal MHD model. However, we do not observe any highly-collimated, high-velocity ($\sigma_{1D} \gtrsim 10$ km s $^{-1}$) outflows in any of our models without sub-grid jet feedback, necessitating the use of the sub-grid model to capture some of the dynamical effects caused by high-velocity jet feedback. Additionally, our sink particle prescription and mass resolution of $\Delta m = 10^{-5} M_\odot$ mean that we do not resolve the star-disk interaction boundary. As protostellar jets are thought to be launched due to the winding of the magnetic field lines and infall of material at the protostellar surface (Shu et al. 1988; Pelletier & Pudritz 1992), it is likely that our models do not accurately capture coupled jet-disk dynamics, such as the correlation between episodic accretion and outflow events (Arce et al. 2007). Similar studies of protostellar disk formation at comparable resolution (e.g., Wurster et al. 2019; Lebreuil et al. 2024a,b) likewise do not observe self-consistent jet launching and attribute the lack of jets to insufficient numerical resolution, frequent changes in disk orientation due to close encounters, and the lack of coherent magnetic field structure due to turbulent initial conditions.

Self-consistent jet launching has been observed in higher-resolution calculations assuming ideal and resistive (Ohmic) non-ideal MHD (e.g., Tomida et al. 2013; Machida et al. 2020), as well as non-ideal calculations with ambipolar diffusion and the Hall effect (e.g., Wurster & Lewis 2020). However, the non-ideal MHD calculations of Wurster & Lewis (2020) showed that non-ideal MHD tended to suppress magnetically-launched outflows from the stellar core. Given enough initial rotation or turbulence, thermally-launched outflows were observed in the non-ideal MHD models after the formation of the stellar core.

In a companion study to their investigation of the effects of including ambipolar diffusion in calculations of disk formation in $M_0 = 1000 M_\odot$ clouds, Lebreuilly et al. (2024b) also included sub-grid jet feedback using an implementation similar to the STAR-FORGE framework (i.e., a fraction $f_w = 0.3$ of accreted material is launched along the sink angular momentum axis at a fraction $f_K = 0.3$ of the escape velocity). They found that including outflows did not have a significant effect on the disk masses and radii by the time the two models were evolved up to a SFE of 0.1 ($\sim 30\text{--}40$ kyr after the onset of star formation). However, including outflows significantly increased fragmentation and lowered accretion luminosities by roughly an order of magnitude, reducing the disk temperatures by a factor of about 2.

4.3 Comparisons with observations

The disks formed in our models have masses of a few $0.001\text{--}0.1 M_\odot$ and radii of a few $10\text{--}100$ AU, as seen in Figures 11 and 12; given the small sample of disks we do not present more detailed statistics. The VANDAM survey towards a sample of 328 protostars in the Orion molecular clouds (Tobin et al. 2020) measured dust continuum emission and reported average dust disk radii of 45 and 37 AU, as well as average dust disk masses of 26 and $15 M_\oplus$, for Class 0 and Class I sources, respectively (with ages of sources in these classes estimated to be roughly 0.2 and 0.5 Myr; see, e.g., Evans et al. 2009; Dunham et al. 2015). These disks are somewhat more compact and significantly less massive than those formed in our numerical models. However, a number of uncertainties make it difficult to draw direct comparisons between observed and modeled disk sizes. The gas disk masses and radii are measured directly from our simulations and are not post-processed to account for optical depth, observational effects, and instrumental resolution. The disk properties reported by the VANDAM survey, meanwhile, describe only the dust content of the disks, which may not be well-coupled to the gaseous component due to both different dynamics as well as biases and limitations in the attainable resolution. Uncertainties in the dust-to-gas ratio, the spatial distribution of dust grains, and the dust size distribution can lead to large errors in the gas properties inferred from the dust emission, particularly when the flux from dust thermal emission is used to estimate the disk mass (see, e.g., the review by Tsukamoto et al. 2023b). As disks evolve on timescales shorter than the age-spread of star-forming regions, the predicted distribution of disk properties is also likely to depend upon initial conditions and the resulting star cluster age distribution. Given these caveats, our results are broadly in agreement with observations, as well as previous numerical non-ideal MHD studies,

4.4 Caveats in calculating non-ideal MHD resistivities

The efficiency and relative ordering of the non-ideal MHD resistivities depend on microphysical parameters such as the dust grain size

distribution and cosmic ray ionization rate. While we adopt a single dust grain radius $a_g = 0.1 \mu\text{m}$ and fixed cosmic ray ionization rate $\zeta_{\text{CR}} = 10^{-17} \text{ s}^{-1}$ for simplicity, several other studies have investigated the effects of modifying the dust grain properties and/or changing the cosmic ray ionization rate on disk formation. Wurster (2021) used models of simple parametrized disks to predict the effects of different grain size assumptions on the values and relative importance of the non-ideal MHD resistivities, comparing models assuming an MRN (Mathis-Rumpl-Nordsieck; Mathis et al. 1977) distribution at several different magnetic field strengths and with or without cosmic ray attenuation to those using singly-sized dust grains, as commonly used in numerical studies such as this work. While the Hall resistivity was the dominant term throughout the disk in most of these idealized models, the ratios η_O/η_A and $|\eta_H|/\eta_A$ differ by less than a factor of ten throughout a significant fraction ($\sim 30\text{--}90\%$) of the disk, suggesting that, regardless of which term dominates, all three non-ideal MHD effects are relevant when considering the evolution of the disk. Zhao et al. (2021) performed 2D axisymmetric calculations using a modified MRN grain size distribution, fixing the power law index and maximum grain size but varying the minimum grain size, to investigate the effect on disk formation. They found that removing the smallest nanometer-sized grains ($a_g \lesssim 10 \text{ nm}$) promoted disk formation, and that truncating the MRN at different minimum grain sizes led to either a Hall-dominated ($a_{\min} = 0.03 \mu\text{m}$) or ambipolar-dominated ($a_{\min} = 0.1 \mu\text{m}$) regime, with the morphologies and kinematics of the envelope and disk showing clear differences between the two types of collapse. While observations suggest that the smallest grains are rapidly depleted due to grain growth in cold dense cores (e.g., Tibbs et al. 2016), the exact grain size distribution in protostellar environments is still poorly constrained. As dust grains may coagulate and fragment during the gravitational collapse and disk formation phases, however, it is unlikely that the size distribution of grains in the disk resembles that observed in the ISM (Dominik & Tielens 1997; Ormel et al. 2009). Non-ideal MHD studies have only just begun to follow dust grain property evolution (Marchand et al. 2023; Tsukamoto et al. 2023a) but have already shown that these processes can significantly modify the values of the non-ideal MHD resistivities throughout disk formation and evolution. Dust grains are also expected to be distributed differently from the gas in protostellar disks due to processes such as settling and radial drift (Dullemond & Dominik 2004; Miotello et al. 2023; Birnstiel 2024). While we assume that the gas and dust are well-coupled and use a constant gas-to-dust ratio $f_{dg} = 0.01$ in order to calculate the non-ideal MHD resistivities, future studies should take into account dust dynamics and evolving dust grain properties in order to more accurately model non-ideal MHD effects.

However, in addition to considering more detailed microphysics, the fundamental assumptions underlying non-ideal MHD effects in protostellar disk regimes may need to be revisited. Recently, Hopkins et al. (2024) challenged several approximations typically used to derive the standard non-ideal MHD equations in weakly-ionized astrophysical systems such as protostellar disks. They argue that these equations are no longer self-consistent when magnetic gradients become too steep and the implied drift velocities between different charged species exceed the thermal velocities. In the case of superthermal drift velocities, the collision rates used to calculate the non-ideal MHD resistivities, which depend on the thermal velocities but assume negligible relative drift velocities, are incorrect. Superthermal drift velocities also generate micro- and mesoscale plasma instabilities, giving rise to a so-called “anomalous resistivity.” They argue that the leading-order effects of correcting for superthermal drifts amount to modifying the effective collision rates

and adding an approximate anomalous resistivity. These corrections reduce the ambipolar diffusivity and greatly enhance the Ohmic resistivity such that the Hall-dominated regime is effectively eliminated. The non-ideal effects then always act diffusively and not dispersively as with the Hall effect, acting to smooth out magnetic gradients and restore subthermal drift velocities. As protostellar disk conditions typically fall in the Hall-dominated regime, this has significant implications for the relative ordering of the non-ideal terms throughout the disk and calls into question several expected disk behaviors ascribed to the Hall effect, such as the preference for anti-alignment between the disk rotation axis and local magnetic field.

5 SUMMARY

We follow the collapse of a magnetized, turbulent $50 M_{\odot}$ molecular cloud cores under different assumptions of (non-)ideal MHD and protostellar feedback through the formation of stellar systems and disks using the MHD code GIZMO. Our results on disk formation and evolution can be summarized as follows:

- Disks form in all models, with ideal MHD and non-ideal MHD, with and without sub-grid jet feedback. Disruption by jet feedback causes certain disks to be short-lived ($\lesssim 12$ kyr). The disk population is diverse.
- Disk masses of $\mathcal{O}(0.001 - 0.1 M_{\odot})$ and radii of $\mathcal{O}(10 - 100$ AU) are broadly in agreement with observed protostellar disks, given the large uncertainties in dust models and flux-to-mass conversions.
- Disks tend to belong to the most massive stars; smaller disks are likely unresolved in these simulations.
- No disk fragmentation is observed. Disks are stable according to the Toomre Q criterion. Multiple systems form due to core and filament fragmentation.
- We do not observe any significant differences in disk properties between the ideal and non-ideal MHD models. Non-ideal MHD disks may be more massive and somewhat longer-lived. A larger statistical study is necessary to determine whether these differences are significant.
- All disks tend to be relatively well-aligned with the stellar angular momentum axis ($\theta_{\text{rel}} \lesssim 20^\circ$) and have an aspect ratio $q \lesssim 0.2$.
- Disk angular momenta in models without the Hall effect show some tendency to be perpendicular to the local magnetic field. The angular momenta of disks in models with the Hall effect tend to become anti-aligned with the local field with time. Again, larger samples are needed to make any definitive claims.
- Sub-grid protostellar jet feedback increases core fragmentation and reduces the final stellar masses.
- Low-velocity ($\sigma_{1D} \sim 0.5$ km s $^{-1}$), loosely-collimated bipolar outflows are observed in the ideal MHD model. We do not observe any self-consistently launched high-velocity, highly-collimated protostellar jets in any of our models.

ACKNOWLEDGEMENTS

NF acknowledges support from the U.S. Department of Energy, Office of Science, Office of Advanced Scientific Computing Research under Award Number DE-SC0023112. SSRO acknowledges support by NSF 2407522. Calculations and analyses for this paper were performed on the Frontera supercomputer at the Texas Advanced

Computing Center (TACC⁵) under the allocations AST23007 and AST23034. The column density and velocity dispersion figures were made using yt⁶.

DATA AVAILABILITY

The data supporting the plots within this article is available by request to the corresponding authors. A public version of the GIZMO code is available⁷.

REFERENCES

- Adams F. C., Ruden S. P., Shu F. H., 1989, *ApJ*, **347**, 959
 André P., Di Francesco J., Ward-Thompson D., Inutsuka S. I., Pudritz R. E., Pineda J. E., 2014, in Beuther H., Klessen R. S., Dullemond C. P., Henning T., eds, Protostars and Planets VI. pp 27–51 ([arXiv:1312.6232](https://arxiv.org/abs/1312.6232)), doi:[10.2458/azu_uapress_9780816531240-ch002](https://doi.org/10.2458/azu_uapress_9780816531240-ch002)
 Andrews S. M., Wilner D. J., Hughes A. M., Qi C., Dullemond C. P., 2010, *ApJ*, **723**, 1241
 Arce H. G., Shepherd D., Gueth F., Lee C. F., Bachiller R., Rosen A., Beuther H., 2007, in Reipurth B., Jewitt D., Keil K., eds, Protostars and Planets V. p. 245 ([arXiv:astro-ph/0603071](https://arxiv.org/abs/astro-ph/0603071)), doi:[10.48550/arXiv.astro-ph/0603071](https://doi.org/10.48550/arXiv.astro-ph/0603071)
 Bate M. R., 2012, *MNRAS*, **419**, 3115
 Bate M. R., 2018, *MNRAS*, **475**, 5618
 Bate M. R., Bonnell I. A., Price N. M., 1995, *MNRAS*, **277**, 362
 Bate M. R., Bonnell I. A., Bromm V., 2003, *MNRAS*, **339**, 577
 Belloche A., 2013, in Hennebelle P., Charbonnel C., eds, EAS Publications Series Vol. 62, EAS Publications Series. pp 25–66 ([arXiv:1305.0627](https://arxiv.org/abs/1305.0627)), doi:[10.1051/eas/1362002](https://doi.org/10.1051/eas/1362002)
 Birnstiel T., 2024, *ARA&A*, **62**, 157
 Bleuler A., Teyssier R., 2014, *MNRAS*, **445**, 4015
 Bonnell I. A., 1994, *MNRAS*, **269**, 837
 Brandenburg A., Zweibel E. G., 1994, *ApJ*, **427**, L91
 Chiang E. I., Goldreich P., 1997, *ApJ*, **490**, 368
 Clark P. C., Glover S. C. O., Klessen R. S., 2012, *MNRAS*, **420**, 745
 Crutcher R. M., 2012, *ARA&A*, **50**, 29
 Cummings A. C., et al., 2016, *ApJ*, **831**, 18
 Cunningham A. J., Klein R. I., Krumholz M. R., McKee C. F., 2011, *ApJ*, **740**, 107
 Dominik C., Tielens A. G. G. M., 1997, *ApJ*, **480**, 647
 Draine B. T., 1978, *ApJS*, **36**, 595
 Draine B. T., 2011, Physics of the Interstellar and Intergalactic Medium
 Dullemond C. P., Dominik C., 2004, *A&A*, **421**, 1075
 Dullemond C. P., Dominik C., Natta A., 2001, *ApJ*, **560**, 957
 Dunham M. M., et al., 2014, in Beuther H., Klessen R. S., Dullemond C. P., Henning T., eds, Protostars and Planets VI. pp 195–218 ([arXiv:1401.1809](https://arxiv.org/abs/1401.1809)), doi:[10.2458/azu_uapress_9780816531240-ch009](https://doi.org/10.2458/azu_uapress_9780816531240-ch009)
 Dunham M. M., et al., 2015, *ApJS*, **220**, 11
 Evans II N. J., et al., 2009, *ApJS*, **181**, 321
 Federrath C., Schrön M., Banerjee R., Klessen R. S., 2014, *ApJ*, **790**, 128
 Finn M. K., et al., 2022, *AJ*, **164**, 64
 Fitz Axen M., Offner S., Hopkins P. F., Krumholz M. R., Grudić M. Y., 2024, *ApJ*, **973**, 16
 Fujii Y. I., Okuzumi S., Inutsuka S.-i., 2011, *ApJ*, **743**, 53
 Ginski C., et al., 2021, *ApJ*, **908**, L25
 Goicoechea J. R., Pety J., Gerin M., Hily-Blant P., Le Bourlot J., 2009, *A&A*, **498**, 771
 Goodman A. A., Benson P. J., Fuller G. A., Myers P. C., 1993, *ApJ*, **406**, 528
 Gray W. J., McKee C. F., Klein R. I., 2018, *MNRAS*, **473**, 2124

⁵ <http://www.tacc.utexas.edu>

⁶ <https://yt-project.org>

⁷ <http://www.tapir.caltech.edu/phopkins/Site/GIZMO.html>

- Grudić M. Y., Guszejnov D., Hopkins P. F., Offner S. S. R., Faucher-Giguère C.-A., 2021, *MNRAS*, **506**, 2199
- Grudić M. Y., Guszejnov D., Offner S. S. R., Rosen A. L., Raju A. N., Faucher-Giguère C.-A., Hopkins P. F., 2022, *MNRAS*, **512**, 216
- Guszejnov D., Hopkins P. F., 2015, *MNRAS*, **450**, 4137
- Guszejnov D., Hopkins P. F., Krumholz M. R., 2017, *MNRAS*, **468**, 4093
- Guszejnov D., Grudić M. Y., Hopkins P. F., Offner S. S. R., Faucher-Giguère C.-A., 2020, *MNRAS*, **496**, 5072
- Guszejnov D., Grudić M. Y., Hopkins P. F., Offner S. S. R., Faucher-Giguère C.-A., 2021, *MNRAS*, **502**, 3646
- Guszejnov D., Grudić M. Y., Offner S. S. R., Faucher-Giguère C.-A., Hopkins P. F., Rosen A. L., 2022, *MNRAS*, **515**, 4929
- Hacar A., Clark S. E., Heitsch F., Kainulainen J., Panopoulou G. V., Seifried D., Smith R., 2023, in Inutsuka S., Aikawa Y., Muto T., Tomida K., Tamura M., eds, Astronomical Society of the Pacific Conference Series Vol. 534, Protostars and Planets VII. p. 153 ([arXiv:2203.09562](https://arxiv.org/abs/2203.09562)), doi:10.48550/arXiv.2203.09562
- Hansen C. E., Klein R. I., McKee C. F., Fisher R. T., 2012, *ApJ*, **747**, 22
- Hartmann L., Calvet N., Gullbring E., D'Alessio P., 1998, *ApJ*, **495**, 385
- Hirano S., Tsukamoto Y., Basu S., Machida M. N., 2020, *ApJ*, **898**, 118
- Hopkins P. F., 2015, *MNRAS*, **450**, 53
- Hopkins P. F., 2017, *MNRAS*, **466**, 3387
- Hopkins P. F., Grudić M. Y., 2019, *MNRAS*, **483**, 4187
- Hopkins P. F., Raives M. J., 2016, *MNRAS*, **455**, 51
- Hopkins P. F., Grudić M. Y., Wetzel A., Kereš D., Faucher-Giguère C.-A., Ma X., Murray N., Butcher N., 2020, *MNRAS*, **491**, 3702
- Hopkins P. F., et al., 2023, *MNRAS*, **519**, 3154
- Hopkins P. F., Squire J., Skalidis R., Soliman N. H., 2024, *arXiv e-prints*, p. arXiv:2405.06026
- Huang J., et al., 2018, *ApJ*, **869**, L42
- Hubber D. A., Walch S., Whitworth A. P., 2013, *MNRAS*, **430**, 3261
- Isella A., Natta A., 2005, *A&A*, **438**, 899
- Joos M., Hennebelle P., Ciardi A., 2012, *A&A*, **543**, A128
- Joos M., Hennebelle P., Ciardi A., Fromang S., 2013, *A&A*, **554**, A17
- Kainulainen J., Stutz A. M., Stanke T., Abreu-Vicente J., Beuther H., Henning T., Johnston K. G., Megeath S. T., 2017, *A&A*, **600**, A141
- Keith S. L., Wardle M., 2014, *MNRAS*, **440**, 89
- Kim J.-G., Ostriker E. C., Filippova N., 2021, *ApJ*, **911**, 128
- Kim J.-G., Gong M., Kim C.-G., Ostriker E. C., 2023, *ApJS*, **264**, 10
- Krasnopol'sky R., Li Z.-Y., Shang H., 2010, *ApJ*, **716**, 1541
- Kratter K., Lodato G., 2016, *ARA&A*, **54**, 271
- Krumholz M. R., McKee C. F., Klein R. I., 2004, *ApJ*, **611**, 399
- Kuffmeier M., 2024, *Frontiers in Astronomy and Space Sciences*, **11**, 1403075
- Lane H. B., Grudić M. Y., Guszejnov D., Offner S. S. R., Faucher-Giguère C.-A., Rosen A. L., 2022, *MNRAS*, **510**, 4767
- Larson R. B., 1969, *MNRAS*, **145**, 271
- Larson R. B., 1972, *MNRAS*, **156**, 437
- Lebreuilly U., et al., 2024a, *A&A*, **682**, A30
- Lebreuilly U., Hennebelle P., Maury A., González M., Traficante A., Klessen R., Testi L., Molinari S., 2024b, *A&A*, **683**, A13
- Lee Y.-N., Offner S. S. R., Hennebelle P., André P., Zinnecker H., Ballesteros-Paredes J., Inutsuka S.-i., Kruijssen J. M. D., 2020, *Space Sci. Rev.*, **216**, 70
- Lesur G., Kunz M. W., Fromang S., 2014, *A&A*, **566**, A56
- Levermore C. D., 1984, *J. Quant. Spectrosc. Radiative Transfer*, **31**, 149
- Lewis B. T., Bate M. R., 2018, *MNRAS*, **477**, 4241
- Li H.-b., Houde M., 2008, *ApJ*, **677**, 1151
- Liu B., Goree J., Nosenko V., Boufendi L., 2003, *Physics of Plasmas*, **10**, 9
- Lynden-Bell D., Pringle J. E., 1974, *MNRAS*, **168**, 603
- Mac Low M.-M., 1999, *ApJ*, **524**, 169
- Machida M. N., Hirano S., Kitta H., 2020, *MNRAS*, **491**, 2180
- Marchand P., Lebreuilly U., Mac Low M. M., Guillot V., 2023, *A&A*, **670**, A61
- Mathis J. S., Rumpl W., Nordsieck K. H., 1977, *ApJ*, **217**, 425
- Maury A., Hennebelle P., Girart J. M., 2022, *Frontiers in Astronomy and Space Sciences*, **9**, 949223
- McKee C. F., Ostriker E. C., 2007, *ARA&A*, **45**, 565
- Mellon R. R., Li Z.-Y., 2009, *ApJ*, **698**, 922
- Miotello A., Kamp I., Birnstiel T., Cleeves L. C., Kataoka A., 2023, in Inutsuka S., Aikawa Y., Muto T., Tomida K., Tamura M., eds, Astronomical Society of the Pacific Conference Series Vol. 534, Protostars and Planets VII. p. 501 ([arXiv:2203.09818](https://arxiv.org/abs/2203.09818)), doi:10.48550/arXiv.2203.09818
- Mocz P., Burkhardt B., Hernquist L., McKee C. F., Springel V., 2017, *ApJ*, **838**, 40
- Moeckel N., Bally J., 2007, *ApJ*, **656**, 275
- Mouschovias T. C., 1991, *ApJ*, **373**, 169
- Mouschovias T. C., Spitzer L. J., 1976, *ApJ*, **210**, 326
- Nakamoto T., Nakagawa Y., 1994, *ApJ*, **421**, 640
- Neufeld D. A., Wolfire M. G., 2017, *ApJ*, **845**, 163
- Ntormousi E., Hennebelle P., André P., Masson J., 2016, *A&A*, **589**, A24
- Offner S. S. R., Chaban J., 2017, *ApJ*, **847**, 104
- Offner S. S. R., Klein R. I., McKee C. F., Krumholz M. R., 2009, *ApJ*, **703**, 131
- Offner S. S. R., Moe M., Kratter K. M., Sadavoy S. I., Jensen E. L. N., Tobin J. J., 2022, *arXiv e-prints*, p. arXiv:2203.10066
- Ormel C. W., Paszun D., Dominik C., Tielens A. G. G. M., 2009, *A&A*, **502**, 845
- Osterbrock D. E., 1961, *ApJ*, **134**, 270
- Ostriker E. C., 1994, *ApJ*, **424**, 292
- Pandey B. P., Wardle M., 2008, *MNRAS*, **385**, 2269
- Pelletier G., Pudritz R. E., 1992, *ApJ*, **394**, 117
- Pfalzner S., 2013, *A&A*, **549**, A82
- Pineda J. E., et al., 2023, in Inutsuka S., Aikawa Y., Muto T., Tomida K., Tamura M., eds, Astronomical Society of the Pacific Conference Series Vol. 534, Protostars and Planets VII. p. 233 ([arXiv:2205.03935](https://arxiv.org/abs/2205.03935)), doi:10.48550/arXiv.2205.03935
- Pineda J. E., et al., 2024, *A&A*, **690**, L5
- Pinto C., Galli D., 2008, *A&A*, **484**, 17
- Pollack J. B., Hollenbach D., Beckwith S., Simonelli D. P., Roush T., Fong W., 1994, *ApJ*, **421**, 615
- Santos-Lima R., de Gouveia Dal Pino E. M., Lazarian A., 2012, *ApJ*, **747**, 21
- Shu F. H., Lizano S., Ruden S. P., Najita J., 1988, *ApJ*, **328**, L19
- Shu F. H., Tremaine S., Adams F. C., Ruden S. P., 1990, *ApJ*, **358**, 495
- Sierra A., Lizano S., 2020, *ApJ*, **892**, 136
- Solomon P. M., Rivolo A. R., Barrett J., Yahil A., 1987, *ApJ*, **319**, 730
- Tazzari M., et al., 2017, *A&A*, **606**, A88
- Tibbs C. T., et al., 2016, *MNRAS*, **456**, 2290
- Tobin J. J., et al., 2020, *ApJ*, **890**, 130
- Tomida K., Tomisaka K., Matsumoto T., Hori Y., Okuzumi S., Machida M. N., Saigo K., 2013, *ApJ*, **763**, 6
- Tomisaka K., 2014, *ApJ*, **785**, 24
- Toomre A., 1964, *ApJ*, **139**, 1217
- Tsukamoto Y., Machida M. N., Inutsuka S.-i., 2023a, *PASJ*, **75**, 835
- Tsukamoto Y., et al., 2023b, in Inutsuka S., Aikawa Y., Muto T., Tomida K., Tamura M., eds, Astronomical Society of the Pacific Conference Series Vol. 534, Protostars and Planets VII. p. 317 ([arXiv:2209.13765](https://arxiv.org/abs/2209.13765)), doi:10.48550/arXiv.2209.13765
- Ueda T., Okuzumi S., Kataoka A., Flock M., 2023, *A&A*, **675**, A176
- Umebayashi T., Nakano T., 1980, *PASJ*, **32**, 405
- Vaidya B., Mignone A., Bodo G., Massaglia S., 2015, *A&A*, **580**, A110
- Wardle M., 2007, *Ap&SS*, **311**, 35
- Wardle M., Ng C., 1999, *MNRAS*, **303**, 239
- Wurster J., 2016, *Publ. Astron. Soc. Australia*, **33**, e041
- Wurster J., 2021, *MNRAS*, **501**, 5873
- Wurster J., Lewis B. T., 2020, *MNRAS*, **495**, 3807
- Wurster J., Li Z.-Y., 2018, *Frontiers in Astronomy and Space Sciences*, **5**, 39
- Wurster J., Price D. J., Bate M. R., 2016, *MNRAS*, **457**, 1037
- Wurster J., Bate M. R., Price D. J., 2019, *MNRAS*, **489**, 1719
- Zhao B., et al., 2020a, *Space Sci. Rev.*, **216**, 43
- Zhao B., Caselli P., Li Z.-Y., Krasnopol'sky R., Shang H., Lam K. H., 2020b, *MNRAS*, **492**, 3375
- Zhao B., Caselli P., Li Z.-Y., Krasnopol'sky R., Shang H., Lam K. H., 2021, *MNRAS*, **505**, 5142
- Zweibel E. G., Josafatsson K., 1983, *ApJ*, **270**, 511

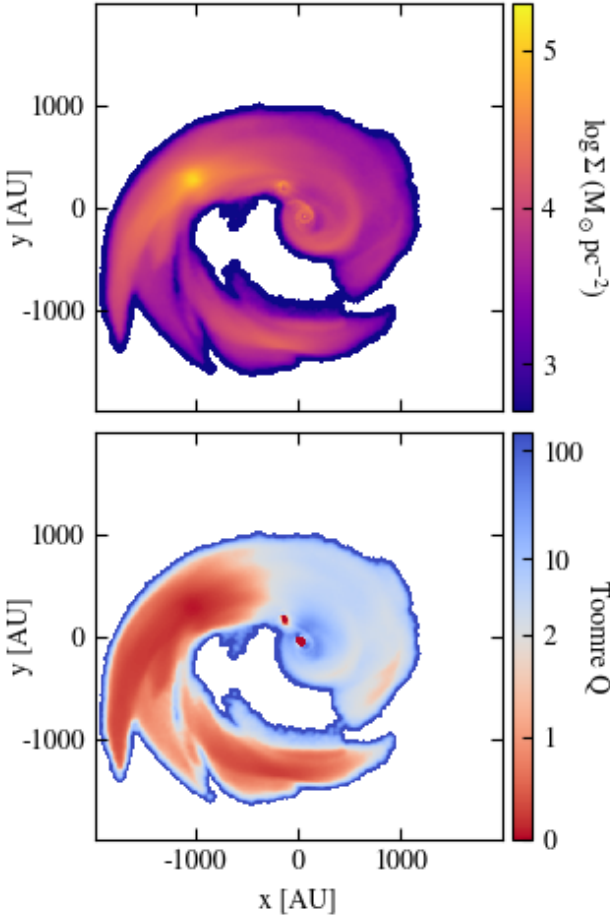


Figure A1. Projected surface density (top) and Toomre Q (bottom) values of the gas with density $n \geq 10^8 \text{ cm}^{-3}$ within 2000 AU of the binary system in the nOA+jets model just prior to the formation of the third star, as shown in the top row of the column density projections in Figure 8. We project along the direction of the net angular momentum of the gas, and use a linear colormap normalization between $Q = 0$ and $Q = 2$ and a logarithmic normalization for $Q > 2$.

APPENDIX A: FRAGMENTING ROTATING ENVELOPE

While we do not observe disk fragmentation in any of our models, we identify a rotating structure extending out to ~ 2000 AU in the non-ideal OA+jets model. This structure is centered around the first two stars to form in this model, and then later fragments to form an additional 3 stars. This structure is not picked out as a disk by our disk identification algorithm when we use a density threshold $n \geq 10^9 \text{ cm}^{-3}$, as in Joos et al. (2012). However, adopting a lower density threshold $n \geq 10^8 \text{ cm}^{-3}$ leads to the identification of this structure as a disk in Keplerian rotation. The top row of Figure A1 shows the surface density of this lower density “disk”, while the bottom row of the figure shows that it is quite gravitationally unstable beyond the inner ~ 1000 AU according to the Toomre Q criterion. Figure A2 shows that the angular velocity profile of this structure is in Keplerian rotation. We identify this structure as part of the rotating envelope material; however, its presence suggests that the boundary between the disk and the envelope might not be as distinct as is typically assumed.

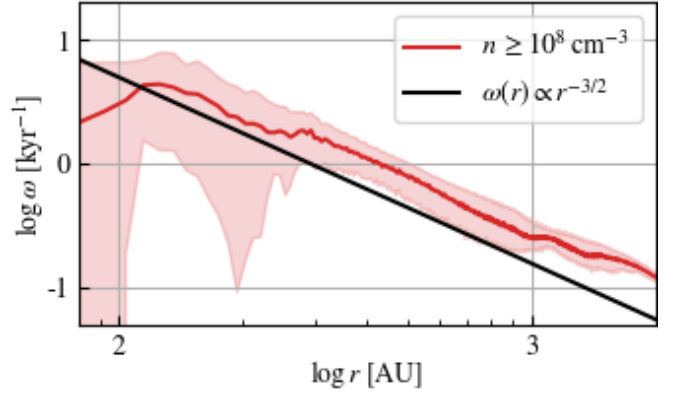


Figure A2. Angular velocity profile of the gas with density $n \geq 10^8 \text{ cm}^{-3}$ within 2000 AU of the binary system in the nOA+jets model just prior to the formation of the third star, as shown in the top row of the column density projections in Figure A2. The shaded region encloses the 5th and 95th percentiles. The black line indicates Keplerian rotation, $\omega(r) \propto r^{-3/2}$.

This paper has been typeset from a TeX/LaTeX file prepared by the author.